JAERI-M
87-056

EVALUATION OF THE OXIDATION BEHAVIOR AND STRENGTH
OF THE GRAPHITE COMPONENTS IN THE VHTR (I)
-NORMAL OPERATION CONDITION-

April 1987

Motokuni ETO, Takeshi KUROSAWA, Shinzo NOMURA
and Hisashi IMAI

EVALUATION OF THE OXIDATION BEHAVIOR AND STRENGTH
OF THE GRAPHITE COMPONENTS IN THE VHTR (I)
— NORMAL OPERATION CONDITION —

Motokuni ETO[+], Takeshi KUROSAWA, Shinzo NOMURA
and Hisashi IMAI

Department of Fuels and Materials Research
Tokai Research Establishment
Japan Atomic Energy Research Institute
Tokai-mura, Naka-gun, Ibaraki-ken

Oxidation experiments have been carried out mainly on a fine-grained isotropic graphite, IG-110, at temperatures between 1173 and 1473 K in a water vapor/helium mixture. In most cases water vapor concentration was 0.65 vol% and helium pressure, 1 atm. Reaction rate and burn-off profile were measured using cylindrical specimens. On the basis of the experimental data the oxidation behavior of fuel block and core support post under the condition of the VHTR operation was estimated using the first-order or Langmuir-Hinshelwood equation with regard to water vapor concentration.

Strength and stress-strain relationship of the graphite components with burn-off profiles estimated above were analyzed on the basis of the model for stress-strain relationship and strength of graphite specimens with density gradients. The estimation indicated that the integrity of the components would be maintained during normal reactor operation.

+ Department of High Temperature Engineering

高温ガス炉用黒鉛構造物の酸化挙動と強度（Ⅰ）

－通 常 運 転 時 の 場 合－

日本原子力研究所東海研究所燃料工学部

衛藤 基邦[+]・黒沢 武・野村 真三・今井 久

ヘリウム中における水蒸気酸化データを主として微粒等方性黒鉛ＩＧ－110 について取得した。温度は1173Ｋから1473Ｋまでとし，水蒸気濃度は主として0.65vol％，ヘリウム圧力は1気圧とした。反応速度と酸化プロファイルを円柱状試験片を用いて測定した。これらの実験結果に基づいて，高温ガス炉内の燃料ブロックと炉心支持ポストの通常運転時における酸化挙動を推定した。その際水蒸気濃度に関する補正は1次式またはLangmuir－Hinshelwood 式を用いた。

上記の黒鉛構造物の寿命期間後の強度と応力－ひずみ関係を別途提出した酸化の影響に関するモデルから推定し，これらの構造物の健全性を明らかにした。

東海研究所：〒 319-11 茨城県那珂郡東海村白方字白根 2 － 4

＋ 高温工学部

CONTENTS

目　　　次

1. INTRODUCTION

It is widely known that the graphite components in the HTGRs are subjected to impurity oxidants in the helium coolant during normal reactor operation or they might be exposed to air or water vapor in an accident that leads to depressurization[1]. Although there have been a number of studies on the oxidation and its effect on various properties of HTGR graphites[2-5], few have dealt with the the details of the oxidation and its effect on the materials properties in the VHTR condition where the oxidation proceeds, in most cases in a manner in which density gradients are resulted from.

The present report consists of three parts which are closely related to each other. In the first part the experimental work on the effect of oxidation on mechanical properties of HTGR graphites is reviewed both for chemical reaction control and in-pore diffusion control regimes, the latter of which would result in oxidation gradients within the graphite component.

Figure 1 shows a schematic of three typical control regimes corresponding to oxidation temperature, i.e., modes (I), (II) and (III) represent the chemical reaction control, in-pore diffusion control and boundary layer control, respectively. Here, C_g is the concentration of gaseous oxidant and R, radius of cylindrical specimen. Regimes (a) and (b) describe the intermediate ranges.

The second part of the report deals with the oxidation behavior of HTGR graphites in detail. First, the experimental data will be analyzed with regard to the reaction rate equation, temperature and burn-off dependences of the oxidation rate, burn-off profile within a specimen, and the effect of irradiation on the rate. Second, the inpile oxidation of graphite will be estimated on the basis of the data obtained in the out-of-pile experiments using the first order or Langmuir-Hinshelwood type equation (L-H eqn.). Third, the above procedures will be applied to the fuel block and core support post used in the VHTR to evaluate the burn-off profile and other oxidation characteristics of the components after their sevice lives.

In the third part the models derived from the experimental data on the strength and stress-strain relationship presented in the first part will be applied to the estimated burn-off profiles within the graphite components of the VHTR in order to evaluate the integrity of these

components during reactor operation.

Figure 2 is a flow sheet describing the above procedures where the case for normal operation is dealt with in this report and that for the water ingress accident will be considered in a separate one to be published soon[6].

2. MECHANICAL PROPERTIES OF OXIDIZED HTGR GRAPHITES

In this section data on the effect of uniform oxidation on mechanical properties of HTGR graphites are reviewed from the aspects of the kind of oxidant and temperature. Then the strength and stress-strain relationship of non-uniformly oxidized graphite will be discussed on the basis of the results on the uniform oxidation.

2.1 Property Changes Caused by Uniform Oxidation

2.1.1 General trend of strength loss of the oxidized graphite

General features of strength decrease of HTGR graphites caused by oxidation are discussed here to give a foothold for the estimation carried out in the following parts on the oxidation behavior of the graphite components.

Effect of oxidation on mechanical properties of VHTR candidate graphites has recently summerized, giving the following conclusions.

(1) The amount of strength loss due to oxidation is different from one graphite to another, although many graphites showed about 50% decrease in strength at a density change level of 10%. Figure 3 is an example of the results where change in bending strength is plotted as a function of density change for IG-110 graphite specimens oxidized in different conditions.

(2) Some graphites showed the larger strength loss comparing with other graphites oxidized to the same burn-off levels. A typical example is shown in Fig. 4 for P3JHA graphite oxidized in air or in a water vapor/helium mixture.

(3) It seems that the amount of strength loss does not depend on the kind of oxidants and oxidant concentrations as long as the oxidation proceeds in the chemical reaction control regime, which is suggested from the results shown in Figs. 3 and 4.

components during reactor operation.

Figure 2 is a flow sheet describing the above procedures where the case for normal operation is dealt with in this report and that for the water ingress accident will be considered in a separate one to be published soon[6].

2. MECHANICAL PROPERTIES OF OXIDIZED HTGR GRAPHITES

In this section data on the effect of uniform oxidation on mechanical properties of HTGR graphites are reviewed from the aspects of the kind of oxidant and temperature. Then the strength and stress-strain relationship of non-uniformly oxidized graphite will be discussed on the basis of the results on the uniform oxidation.

2.1 Property Changes Caused by Uniform Oxidation

2.1.1 General trend of strength loss of the oxidized graphite

General features of strength decrease of HTGR graphites caused by oxidation are discussed here to give a foothold for the estimation carried out in the following parts on the oxidation behavior of the graphite components.

Effect of oxidation on mechanical properties of VHTR candidate graphites has recently summerized, giving the following conclusions.

(1) The amount of strength loss due to oxidation is different from one graphite to another, although many graphites showed about 50% decrease in strength at a density change level of 10%. Figure 3 is an example of the results where change in bending strength is plotted as a function of density change for IG-110 graphite specimens oxidized in different conditions.

(2) Some graphites showed the larger strength loss comparing with other graphites oxidized to the same burn-off levels. A typical example is shown in Fig. 4 for P3JHA graphite oxidized in air or in a water vapor/helium mixture.

(3) It seems that the amount of strength loss does not depend on the kind of oxidants and oxidant concentrations as long as the oxidation proceeds in the chemical reaction control regime, which is suggested from the results shown in Figs. 3 and 4.

(4) It is found that the larger the strength loss, the larger the resistivity increase due to oxidation. Decrease in bending strength per % density change is shown in Fig. 5 as a function of resistivity increase per % density change.

In the following sections results on mainly IG-110 graphite will be discussed because the reaction rate and burn-off profile of this material are to be dealt with in the following parts. The material is considered to be the most promising candidate for the core and core support components. Moreover, from the argument described above and the data shown in the references[5], the basic idea shown below is believed to be applicable to any kind of nuclear graphite if some necessary modifications regarding the reaction rate, burn-off profile and strength decrease are made for each graphite concerned.

2.1.2 Stress-strain relationship

Compressive stress-strain curves for IG-110 graphite oxidized in air to various burn-off levels are shown in Fig. 6. The previous reports[7-9] indicated that the strength loss can be related with the density change as

$$\frac{\sigma_f}{\sigma_{fo}} = (\frac{\rho}{\rho_o})^n \tag{1}$$

The value of n ranged from 4.3 to 6.2 depending on the kind of strength measured and burn-off level. The equation of this type has also been widely used to express the relationship between strength decrease and density change caused by oxidation for other HTGR graphites.

From the results shown in Fig. 6 an empirical equation concerning the stress-strain relationship was derived for both tension and compression. From the experimental data obtained so far, the following equation was obtained.

$$\frac{\sigma(\epsilon)}{\sigma_o(\epsilon)} = (\frac{\rho}{\rho_o})^m \tag{2}$$

Here, $\sigma(\epsilon)$ and $\sigma_o(\epsilon)$ are stresses at strain ϵ for the oxidized and un-oxidized materials, respectively[5]. The values of m were 4.56 and 3.95 for compression and tension, respectively. An example of the data from which the above equation was derived is shown in Table 1 where the ratio of compressive stress for the oxidized to that for the unoxidized specimens

are summerized for IG-110 graphite oxidized in air at 773 K to various burn-off levels.

2.2 Stress-Strain Relationship and Strength of Graphite with Oxidation Gradient

On the basis of the empirical equations obtained in Section 2.1 stress-strain relationship and strength of graphite with oxidation gradient, i.e., density gradient will be discussed here. An analytical formula is introduced and compared with the experiments[7-9].

2.2.1 Stress-strain relationship

Let us consider a cylindrical specimen with a density gradient due to oxidation in Fig. 6. Assuming that a hollow tube with inner and outer radii r and r + dr, respectively, has density ρ as shown in Fig. 7 and that the compressive stress exerted perpendicular to the cross-section of the hollow tube is σ, we obtain $dP = \sigma 2\pi r \, dr$ for the external load applied to this part. Thus, for the total applied load,

$$P = \int \sigma 2\pi r \, dr \tag{3}$$

provided that r is expressed as a function of ρ, i.e.,

$$r = f(\rho) \tag{4}$$

P can be rewritten, from Eqns(3) and (4),

$$P = \int_{\rho_c}^{\rho_s} 2\pi\sigma f(\rho) \, d\rho \tag{5}$$

where ρ_s and ρ_c are densities at the surface and center of the cylindrical specimen, respectively. From Eqn (2),

$$\sigma(\varepsilon) = A \, \sigma_0 \, (\varepsilon) \, \rho^m \tag{6}$$

where A is expressed as $A = \rho_0^{-m}$. Substituting Eqn (6) into Eqn (5), we get

$$P = \sigma_o (\varepsilon) \ 2\pi A \int_{\rho_c}^{\rho_s} \rho^m \ f(\rho) \ f'(\rho) \ d\rho \qquad (7)$$

Thus the stress-strain relationship with the density gradient whose profile is shown in Fig. 7 can be given by

$$\sigma(\varepsilon) = P / \pi r_s^2 \qquad (8)$$

where r_s is the outer radius of the specimen.

Results of the calculation for the cylindrical specimens with burn-off profiles shown in Fig. 8(a) are seen in Fig. 8(b) in comparison with the experimental data. It is found that there is good agreement between the calculation and experiment. Results similar to this were obtained for tensile stress-strain curves. An example is shown in Figs. 8(c) and (d).

2.2.2 Prediction of strength of graphite with density gradient

Strength of specimen with the density gradient shown in Fig. 7 has been estimated on the basis of a model shown below[10].

When the external load P is applied to the cross-sectional area of the specimen, the deformation along the loading axis is believed to be uniform within the cross-section. However, the stress exerted perpendicular to the cross-section varies depending on the location within the cross-section. From Eqn(1) fracture strength at the exterior of such a specimen is always smaller than that of the interior adjacent to the exterior.

We consider the infinitesmal layer with density and strength of the region adjacent to that at radius r to which the partial fracture has already extend, and assume that the fracture strain of the exterior is always smaller than that of the interior. Whether or not the partial fracture of the layer extends toward the interior region is determined by the following relationship.

$$\frac{P}{\pi r^2} \geq \sigma_f \qquad (9)$$

Taking account of the fact that the layer at radius r has a density of ρ, Eqn(9) can be written as

$$\frac{P}{\pi r^2} \geq \sigma_{fo} \left(\frac{\rho}{\rho_o} \right)^n \tag{10}$$

Since ρ can be represented as a function of r, i.e., from Eqn(4), $\rho = g(r)$, Eqn(10) can be expressed as

$$P \geq \sigma_{fo} \, \pi r^2 \quad (g(r)/\rho_o)^n \qquad Q(r) \tag{11}$$

Thus, the strength of the specimen is believed to be estimated by fitting the maximum of $Q(r)$ in Eqn(11) with respect to r.

Fig. 9 shows some results of the calculation of compressive strength carried out for several specimens 24mm in diameter and 48mm in length oxidized in air at 773 K to burn-off levels of 4.8, 12.2, 19.5 and 29.5 % for specimens C, D, E and F, respectively. The largest difference between the experimental and the predicted was 20 %. The argument described here will be considered when the strength of the graphite components is estimated later.

3. ANALYSIS OF OXIDATION BEHAVIOR OF HTGR GRAPHITES

First, results of the experiments on HTGR graphites oxidized in water vapor/helium mixtures are shown here. Then the reaction rate, weight loss and burn-off profile in the condition of VHTR operation are estimated on the basis of these results. That is, the experimental data will be modified in consideration of

1) dependence of reaction rate on the concentration of oxidant and total pressure,
2) effect of helium pressure and flow rate,
3) burn-off dependence of the reaction rate,
4) effects of γ-ray and neutron irradiation,
5) catalyzing effect of impurities and fission products, and
6) evaluation of the data scatter.

A computer code has been developed for the above calculation. Flow diagram of the code is shown in Appendix 2.

$$\frac{P}{\pi r^2} \geq \sigma_{fo} \left(\frac{\rho}{\rho_o} \right)^n \qquad (10)$$

Since ρ can be represented as a function of r, i.e., from Eqn(4), $\rho = g(r)$, Eqn(10) can be expressed as

$$P \geq \sigma_{fo} \pi r^2 \quad (g(r)/\rho_o)^n \qquad Q(r) \qquad (11)$$

Thus, the strength of the specimen is believed to be estimated by fitting the maximum of $Q(r)$ in Eqn(11) with respect to r.

Fig. 9 shows some results of the calculation of compressive strength carried out for several specimens 24mm in diameter and 48mm in length oxidized in air at 773 K to burn-off levels of 4.8, 12.2, 19.5 and 29.5 % for specimens C, D, E and F, respectively. The largest difference between the experimental and the predicted was 20 %. The argument described here will be considered when the strength of the graphite components is estimated later.

3. ANALYSIS OF OXIDATION BEHAVIOR OF HTGR GRAPHITES

First, results of the experiments on HTGR graphites oxidized in water vapor/helium mixtures are shown here. Then the reaction rate, weight loss and burn-off profile in the condition of VHTR operation are estimated on the basis of these results. That is, the experimental data will be modified in consideration of

1) dependence of reaction rate on the concentration of oxidant and total pressure,

2) effect of helium pressure and flow rate,

3) burn-off dependence of the reaction rate,

4) effects of γ-ray and neutron irradiation,

5) catalyzing effect of impurities and fission products, and

6) evaluation of the data scatter.

A computer code has been developed for the above calculation. Flow diagram of the code is shown in Appendix 2.

3.1 Results of the Out-of-Pile Experiments

3.1.1 Reaction rate equation

IG-110 graphite specimens 11 mm in diameter and 50 mm in length were oxidized in a 0.65 % water vapor/helium mixture at atmospheric pressure at a flow rate smaller than 100 mm/s. Reaction rate was measured in the temperature range from 1073 to 1523 K.

From the Arrhenius plot of the data shown in Figs. 10 and 11, the following equations were obtained:

$$R_e = 4.5 \times 10^4 \exp(-113/RT) \tag{12}$$

for temperatures above about 1200 K,

$$R_e = 1.8 \times 10^{10} \exp(-251/RT) \tag{13}$$

for temperatures below about 1200 K. Here, R_e represents the reaction rate (weight loss per unit exterior surface area per unit time, $mg/cm^2 \cdot h$) at a given weight loss per unit exterior surface area $B(mg/cm^2)$. The figures in the exponential terms are apparent activation energy for the reaction expressed in unit of kJ/mol.

It was found in these experiments that the temperature above which the reaction proceeded in the in-pore diffusion control regime was about 1200 K. Below this temperature the reaction rate was controlled mainly by the reactivity of graphite.

3.1.2 Burn-off dependence of reaction rate

The burn-off dependence of reaction rate was examined at temperatures of 1273, 1373 and 1473 K. Change in reaction rate at each temperature was expressed as a function of B, weight loss per unit exterior surface area in unit of mg/cm^2, i.e., F(B). Figure 12 shows the burn-off dependence of the reaction rate which was normalized to that at B = 15. As for the rate at temperatures lower than 1273 K the values in the reference[11] were employed.

3.1.3 Burn-off profile within a specimen oxidized at different
       temperatures

Figure 13 shows examples of the results obtained for several kinds
of graphites[12]. Cylindrical specimens 50 mm in diameter were oxidized
at 1273 K in a water vapor/helium mixture flow at the atmospheric
pressure. The local burn-off represented by bulk density, ρ, at a
distance from the exterior surface, x, in the radial direction is
expressed as

$$\frac{\rho_o - \rho}{\rho_o} = \frac{\Delta\rho}{\rho_o} = A \exp\left(-\frac{x}{L}\right) \tag{14}$$

Here, ρ_o and A are the bulk density of unoxidized specimen and burn-off
at x = 0 of oxidized specimen, respectively. L, the characteristic length
of oxidation was found to be 1.7 mm for IG-110 graphite. For temperatures
between 1173 and 1273 K,

$$L \text{ (mm)} = 3.89 \times 10^{-6} \exp(16500/T) \tag{15}$$

3.2 Reaction Rate in the In-Pile Condition

The rate equation for the reaction of graphite in the VHTR condition,
R_p, was derived multiplying R_e by various compensation factors, i.e.,

$$R_p = F(P,C_{H_2O},T) \ I \ J \ I_n \ I_\gamma \ F(M) \ F(B) \ R_e \tag{16}$$

Here, F(P,C,T) : Factor regarding total pressure, water vapor
                   concentration and temperature

        I : Compensation factor regarding helium flow rate

      I_n : Factor regarding neutron-irradiation effect

      I_γ : Factor regarding γ-ray irradiation effect

     F(M) : Factor regarding the effect of impurities

     F(B) : Factor regarding the burn-off dependence of rate

3.2.1 Dependence of reaction rate on the concentration of
       oxidant and total pressure

Here, the effects of total pressure and water vapor concentration on
the reaction rate in the chemical reaction control regime were considered

for the following two cases: (1) the rate is proportional to the water vapor concentration as long as the the total pressure is the same (First order equation) and (2) the rate obeys Langmuir-Hinshelwood type equation.

At higher temperatures the reaction is governed by mass transport of reacting gas across a relatively stagnant gas film between the exterior surface of the solid and the main gas stream (boundary layer diffusion control regime). The experimental data shown in this report, however, were obtained mainly in the in-pore diffusion and the chemical reaction control regimes so that these two types of regimes will be analyzed here.

1) First order equation

R_p was estimated from the following equation.

$$R_p = P^n \, C_r \, H \, I \, J \, I_n \, I_\gamma \, F(M) \, F(B) \, R_e \qquad (17)$$

Here, P : Total pressure

　　　n : n=1 for chemical reaction control regime, 1/2 for the in-pore diffusion control regime

　　　C : Reduced water vapor concentration (vpm)

　　　H : Compensation factor regarding water vapor concentration.

From the assumption that the rate is proportional to the partial pressure of water vapor, the rate R_p is proportional to $(P \, C_{H_2O}/6500) \, R_e$ in the chemical reaction control regime, where C_{H_2O} is water vapor concentration in vpm and 6500 is that in vpm for the present experiment. Hence, $C_{H_2O}/6500$ is C_r in this case.

In the in-pore diffusion control regime, however, the rate is influenced by effective diffusion of gases through pores of graphite. Since the effective diffusion constant, D_{eff} is proportional to $1/P$ and the rate is proportional to $D_{eff}^{1/2}$ at the same temperature, the rate is proportional to $P^{-1/2}$[13]. The partial pressure multiplied by this effect of total pressure is shown by $P^{-1/2} \, P \, C_{H_2O}$. n are 1/2 for the in-pore diffusion control regime and 1 for the chemical reaction control regime, as also reported by Everett et al.[14].

H is a compensation factor for the fact that the relative reaction rate per unit water vapor partial pressure increases with decreasing partial pressure itself. Fig. 14 shows the reaction rate as a function of partial pressure[15]. A value of 1.2 was chosen for H on the basis of

this figure. On the other hand, when water vapor partial pressure is higher than 2.4 atm as in the case of water ingress accident, H is smaller than unity. Another treatment of reaction rate as a function of water vapor partial pressure will be described in more detail in the next section and in the next report which deals with the accident condition[6].

2) Langmuir-Hinshelwood type equation (L-H eqn.)

In the previous description of the first order equation it has been assumed that the reaction rate is proportional to the first order of water vapor partial pressure, and that in the in-pore diffusion control regime the rate is proportional to the reciprocal of the square root of the total pressure, whereas in the chemical reaction control regime the rate is independent of total pressure.

For the prediction of the reaction rate in use of Langmuir-Hinshelwood equation, compensation factors such as P, n, C_r, and H are replaced with a function of total pressure, water vapor concentration and temperature, $F(P, C_{H_2O}, T)$, i.e., the reaction rate is expressed as

$$R_p = F(P, C_{H_2O}, T) \ I \ J \ I_n \ I_\gamma \ F(M) \ F(B) \ R_e \qquad (18)$$

(1) Langmuir-Hinshelwood equation in the chemical reaction control regime

It is widely known that the experimental data on the rate for the chemical reaction of graphite with water vapor,

$$C + H_2O = H_2 + CO , \qquad (19)$$

can be fitted to the Langmuir-Hinshelwood equation of the form[16],

$$K = \frac{k_1 P_{H_2O}}{1 + k_2 P_{H_2} + k_3 P_{H_2O}} \qquad (20)$$

where P_{H_2O} and P_{H_2} are the partial pressures of H_2O and H_2, respectively.

In the chemical reaction control regime we define $F(P, C_{H_2O}, T)$ from K-value calculated for the experimental condition, K_e and that for the reactor operation condition, K_p, as

$$F(P, \ C_{H_2O}, \ T) \ = \ \frac{K_p}{K_e} \tag{21}$$

The constants k_i's $(i=1,2,3)$ in Eqn.(20) are rate constants for the elementary processes. Although hydrogen decreases the reaction rate, this effect was not taken into account here. The neglect of the effect gives the more conservative estimation of the rate for the reactor operation condition. Introducing a parameter Y which is defined below, we obtain $F(P, \ C_{H_2O}, \ T)$ as

$$Y \ = \ \frac{P \ C_{H_2O}}{1 + k_3 P C_{H_2O}} \tag{22}$$

$$F(P, \ C_{H_2O}, \ T) \ = \ \frac{Y_p}{Y_e} \tag{23}$$

provided the temperature is the same. Here, Y_e and Y_p are the Y-values for the experimental and in-pile conditions, respectively. The reaction rate in the reactor operation condition, R_p can be estimated using Eqns. (18) and (23).

(2) Langmuir-Hinshelwood equation for the in-pore diffusion
    control regime

    For analyzing the reaction in the in-pore diffusion control regime
Y was determined as

$$Y \ = \sqrt{\frac{1}{2} \ \{P_{H_2O} - \frac{1}{k_3} \ \log(k_3 P_{H_2O} + 1)\}} \tag{24}$$

The details of the derivation of Eqn.(24) and the following Eqn. (25) will be shown in Appendix 1. Here as described in the former section, the effect of hydrogen was neglected in the derivation of Y. Calculations of Y for the experimental condition, Y_e and that for the reactor operation condition Y_p give rise to F as

$$F \ (P, \ C_{H_2O}, \ T) \ = \ \frac{Y_p}{Y_e} \tag{25}$$

R can be calculated using Eqns.(18) and (25).

3.2.2 Effect of helium flow rate

I in the Eqn.(16) is a compensation factor for the effect of helium flow rate. The result of Burnette et al[17] on H-451 in a simulated HTGR condition using a high-pressure test loop (HPTL) was compared with H-451 data obtained in our experiment. The comparison indicated that the rate obtained at the high flow rate was 1.2 times as large as that obtained at temperatures between 1088 and 1213K in our experiment. Since there have been few data available on the effect of flow rate on the reaction rate from the aspects of temperature, burn-off and kind of graphite, a value of 1.2 was adopted for compensation the flow rate effect on the reaction rate.

3.2.3 Burn-off dependence of the reaction rate

F(B) is a factor regarding the burn-off dependence of reaction rate. In most cases, the reaction rate increases with increasing burn-off. As was mentioned in 3.1.2, the changes in the reaction rate as a function of B were measured at a temperature of 1273, 1373 or 1473 K. Here, F(B) curves were obtained normalizing the reaction rate values to those at B=15 as is seen in Fig.12. The rate expressed as Eqns.(12) and (13) is that at B=15. As for the F(B) curves for temperatures lower than 1273 K, the values in the reference[1] were employed.

The curves were fitted to polynomial functions of B as follows.

F(B) at 1093 K:

$$0 \leq B \leq 40,$$
$$F(B) = 3.33656 \times 10^{-2} + 7.0375 \times 10^{-2} - 1.1751 \times 10^{-5} B^2 -$$
$$- 8.4415 \times 10^{-5} B^3 + 6.5015 \times 10^{-7} B^4 - 4.4887 \times 10^{-9} B^5 \qquad (26)$$
$$B > 40, \quad F(B) = 1.8323 \qquad (27)$$

F(B) at 1173 K:

$$0 \leq B \leq 40,$$
$$F(B) = 2.2711 \times 10^{-1} + 5.932 \times 10^{-2} B - 2.7964 \times 10^{-4} B^2$$
$$- 2.3152 \times 10^{-5} B^3 + 5.4102 \times 10^{-7} B^4 + 4.2759 \times 10^{-9} B^5 \qquad (28)$$
$$B > 40, \quad F(B) = 1.618 \qquad (29)$$

F(B) at 1273 K:

$$0 \leq B < 0.03, \quad F(B) = 1.107 \times 10^{-1} + 3.623 B \qquad (30)$$
$$0.03 \leq B < 0.8, \quad F(B) = 1.963 \times 10^{-1} + 8.722 \times 10^{-1} B - 1.959 B^2$$
$$+ 2.254 B^3 - 9.392 \times 10^{-1} B^4 \qquad (31)$$

$$0.8 \leq B < 60, \quad F(B) = 3.527 \times 10^{-1} + 7.820 \times 10^{-2}B - 3.828 \times 10^{-3}B^2$$
$$+ 1.280 \times 10^{-4}B^3 - 2.092 \times 10^{-6}B^4 + 1.269 \times 10^{-8}B^5$$

(32)

$$B > 60, \quad F(B) = 1.6674$$

(33)

$F(B)$ at 1373 K:

$$0 \leq B < 0.1, \quad F(B) = 1.325 \times 10^{-1} + 1.325 \, B$$

(34)

$$0.1 \leq B < 1,$$
$$F(B) = 2.189 \times 10^{-1} + 5.351 \times 10^{-1}B - 7.100 \times 10^{-1}B^2$$
$$+ 6.472 \times 10^{-1}B^3 - 3.187 \times 10^{-1}B^4 + 6.440 \times 10^{-2}B^5$$

(35)

$$1 \leq B \leq 60,$$
$$F(B) = 3.623 \times 10^{-1} + 8.152 \times 10^{-2}B - 4.068 \times 10^{-3}B^2$$
$$+ 1.239 \times 10^{-4}B^3 - 1.907 \times 10^{-6}B^4 + 1.125 \times 10^{-8}B^5$$

(36)

$$B > 60, \quad F(B) = 1.4045$$

(37)

$F(B)$ at 1473 K:

$$0 \leq B < 0.2, \quad F(B) = 1.912 \times 10^{-1} + 9.562 \times 10^{-1}B$$

(38)

$$0.2 \leq B < 3,$$
$$F(B) = 2.297 \times 10^{-1} + 9.130 \times 10^{-1}B - 8.338 \times 10^{-1}B^2$$
$$+ 3.697 \times 10^{-1}B^3 - 7.496 \times 10^{-2}B^4 + 5.610 \times 10^{-3}B^5$$

(39)

$$3 \leq B < 60,$$
$$F(B) = 5.844 \times 10^{-1} + 5.638 \times 10^{-2}B - 3.090 \times 10^{-3}B^2$$
$$+ 9.796 \times 10^{-5}B^3 - 1.212 \times 10^{-6}B^4 - 1.068 \times 10^{-8}B^5$$

(40)

$$B > 60, \quad F(B) = 1.2317$$

(41)

3.2.4 Effects of γ-ray and neutron irradiations

With regard to the irradiation effects, i.e., I_γ and I_n, it was reported that the contribution from radiolytic reaction to the overall reaction rate was small enough to neglect at temperatures above about 1050K[18,19]. The radiolytic reaction rate was much smaller than the thermal reaction rate at higher temperatures. The total reaction rate was, therefore, virtually equal to the thermal reaction rate. The ratio of the radiolytic reaction rate to the thermal one increased with decreasing temperature so that at much lower temperatures the radiolytic oxidation exceeded the thermal one. However, the effect of γ-ray irradiation can be disregarded for the temperature range concerned in this report.

A result of reaction rate measurements for neutron-irradiated specimens is shown in Fig.15 where one can see that the irradiation does

not affect the reaction rate. The effect of neutron-irradiation was also neglected, i.e., $I_n = 1$.

3.2.5 Catalyzing effect of impurities and fission products

F(M) is a factor regarding the effect of impurities in graphite. It is well known that impurities have an catalytic effect on the reaction, i.e., almost all impurities accelerate the reaction rate. The effect of impurities depends on many factors such as species, distribution and chemical state especially concentration. Since the metallic impurities remain in the oxide form on the graphite crystallite surface during the reaction, the concentration of metallic impurities on the surface increases with proceeding of the reaction. However, such effect is included in the burn-off dependence of the reaction rate.

Besides impurities, fission products are believed to affect the reaction rate in the reactor operation condition. Among fission products, Ba and Sr are known to have large catalytic effect accelerating the reaction process. However, the concentrations of accumulated Ba and Sr were estimated to be less than 0.1 ppm in the fuel matrix when a failure probability of coated fuel particles was assumed to be 10^{-3} after reactor operation of 400 days[20]. Since the concentration in the structural graphite components is to be far below 0.1 ppm so that the catalytic effect caused by fission products was neglected, i.e., F(M) = 1.

3.2.6 Evaluation of the data scatter

J is a factor representing the upper limit of the scatter of the reaction rate. The standard deviation, σ of the reaction rates shown in Figs. 10 and 11 is 1/6 of the mean value. The mean value plus 2σ was supposed to be the upper limit of the reaction rate so that a value of 4/3 was chosen for J. The J-value employed here is believed to be conservative enough for estimating the reaction rate in the in-pile condition.

3.3 Estimation of the Transient Temperature

As was mentioned in 3.1.1, the transition temperature was found to be around 1200K in the experiment. This temperature depends on total pressure. Since the reaction rate changes continuously with regard to temperature, the reaction rates in the chemical reaction control and

in-pore diffusion control regimes should be equal to each other at the transition temperature, i.e.,

$$R_{p.i} = R_{p.c} \tag{42}$$

Here, c and i denote that the values are calculated in the chemical reaction control and the in-pore diffusion control regimes, respectively. In this report, Eqn.(17) was adopted for calculating the transition temperature. Since all the compensation factors except n, I, F(B) are equal both for the chemical reaction control and in-pore diffusion control regimes, respectively, from the above equation the following expression can be obtained:

$$\frac{(P^n \cdot I \cdot F(B) \cdot R_e)_c}{(P^n \cdot I \cdot F(B) \cdot R_e)_i} = 1 \tag{43}$$

Since at the temperature range (ca.1100-1500 K) with which our estimation is concerned the effect of irradiations was neglected, the above equation can be applicable to the experimental data obtained in the chemical reaction control regime, which was shown in 3.1.

Let $T_{tr.e}$ and $T_{tr.p}$ represent the transition temperature in the experimental condition and in-pile condition, respectively. For a given B, $T_{tr.p}$ is derived from the equations,

$$T_{tr.p} = T_{tr.p} \left(1 - \frac{1}{1 + \dfrac{Ec - Ei}{R \cdot T_{tr.e} \cdot \ln(Y)}} \right) \tag{44}$$

$$Y = \frac{(P^n \cdot I)c}{(P^n \cdot I)i} \tag{45}$$

Here, E_c and E_i are the apparent activation energies for the reaction in the chemical reaction control and in-pore diffusion control regimes, respectively.

$T_{tr,p}$ estimated in a manner described above was adopted as a criterion for determining to which of the two rate-controling steps the reaction belongs.

3.4 Calculation of Reaction Rate, Weight Loss and Burn-off Profile

Here, the calculation was made for the normal operation condition, whereas the water ingress accident will be discussed in a separate report[6] following processes similar to that described below.

3.4.1 Calculation of changes in the reaction rate and weight loss as a function of time

(1) Material and parameters for the calculation under normal reactor operation condition

Reaction rate and weight loss were estimated for the fuel block and core support post of IG-110 graphite as a function of time. The parameters used for the calculation were assumed to be as follows.

Rate of operation : 60 %

Service life   : 2 years for fuel block, and 20 years for core support post

Helium pressure : 4 MPa

H_2O concentration : 0.2 vpm

(2) Procedure of the calculation of the changes in the reaction rate and weight loss

1) Basic procedure

R_p at a given B when $F(B) = 1$ is calculated using Eqns.(16) and (17). Let this value represent as $R_{p,ref}$, then R_p at any value of B is expressed as

$$R_p = R_{p,ref} F(B) \qquad (46)$$

Let $R_p(t)$ and $B(t)$ represent R_p and B at time t. Increase of B observed from t to $t+\Delta t$, $B(t \to t+\Delta t)$, is expressed as

$$\begin{aligned} B(t \to t+\Delta t) &= R_p(t)\, \Delta t \\ &= B(t+\Delta t) - B(t) \end{aligned} \qquad (47)$$

In a similar manner,

$$R_p(t \to t+\Delta t) = R_p \text{ at } B = B + \Delta B \qquad (48)$$

$$= R_{p,ref} F(B+\Delta B) \qquad (49)$$

Following the above procedures from $t = 0$ where $B = 0$ to $t + \Delta t$ we obtain the reaction rate and weight loss as a function of time.

2) Modified procedure

The basic procedure above was modified because in this procedure, if time interval Δt is not small enough, the results may be fairly under-estimated ones. The modified procedure enables us to check the results obtained in the basic procedure and obtain the more conservative values. The procedure is as follows.

First: Calculate the reaction rate and weight loss at t according to the above procedure.

Second: Define t'(t) as

$$\Delta t'(t) = \frac{R_p(t)}{R_p(t+\Delta t)} \Delta t \qquad (50)$$

Third: Let the sum of $\Delta t'(t)$ from $t = 0$ to $t = t$ represent as t'(t) which is expressed as

$$t'(t) = \sum_{i=0}^{n-1} \Delta t'(i \cdot \Delta t) \qquad (51)$$

$$= \sum_{i=0}^{n-1} \frac{R_p(i \cdot \Delta t) \cdot \Delta t}{R((i+1) \cdot \Delta t)} \qquad (52)$$

$$t' = n \cdot \Delta t \qquad (53)$$

Fourth: Suppose that the values of reaction rate and weight loss at t'(t), $R_p(t'(t))$ and $B(t'(t))$ are equal to $R_p(t)$ and $B(t)$ respectively, i.e.,

$$R_p(t'(t)) = R(t) \qquad (54)$$
$$B(t'(t)) = B(t) \qquad (55)$$

Then the reaction rate and weight loss at a time t'(t) are given as $R_p(t)$ and $B(t)$, respectively. Here, an assumption was made regarding A-value in Eqn.(14): when A reaches a value larger than 0.9, the reaction would show a constant rate including erosion[12].

3.4.2 Calculation of burn-off profile

Burn-off profile was calculated on the basis of the B-values described above. L in Eqn.(15) can be expressed as $L = \sqrt{D_{eff}/K_v}$[21]. Here, K, rate

constant per unit volume of graphite is constant for a constant temperature. Since $D_{eff} \propto 1/P$, L at P is, from Eqn.(15),

$$L(mm) = 3.89 \times 10^{-6} (1/\sqrt{P}) \exp(16500/T) \tag{56}$$

Also, ΔW_x, weight loss per unit exterior surface area in the region between the exterior surface and the depth x is to be

$$\Delta W_x = d_0 \int_0^x A \exp(-x/L) \, dx = d_0 L A \, 1-\exp(-x/L) \tag{57}$$

where d_0 is bulk density prior to oxidation and A is burn-off at the surface.

If the size of component is larger enough than L, the overall loss of weight per unit exterior surface area, ΔW, is approximately expressed as

$$\Delta W = d_0 L A \tag{58}$$

This equation was used to calculate A-values. The characteristic length of oxidation, L was confirmed to be independent of burn-off[12]. Since $\Delta W(t)$ at time t_x is equal to B(t), A at time t can be expressed as

$$A(t) = B(t)/d_0 L \tag{59}$$

The burn-off profile as a function of time can be calculated from Eqns.(56) and (59).

The dependences of L on water vapor concentration, size and shape of specimen will be discussed in the next report[6]. It was assumed in this report that L does not depend on these parameters. An assumption was also made that, as was described in 3.4.1, erosion would take place for burn-off levels larger than 90%[22].

3.4.3 Results of the calculation
(1) Fuel block

Figs.16(a), (b) and (c) show results of the calculations of reaction rate, weight loss and burn-off profile for the fuel block at 1273K using the first order equation. Figs.17(a), (b) and (c) show results sumilar to those in Fig.16 obtained on the basis of Langmuir-Hinshelwood equation. Burn-off profiles for the oxidation at 1473K are shown in Figs.18 and 19 in

the cases of the first order and Langmuir-Hinshelwood equations, respectively.

(2) Core support post

Burn-off profiles of the core support post calculated at 1273K and 1373L are shown in Figs.20 through 23, where Figs.20 and 21 are the results obtained in use of the first order equation, and the Langmuir-Hinshelwood equation was used in Figs.22 and 23.

4. APPLICATION OF THE STRENGTH LOSS MODEL TO
THE OXIDIZED COMPONENTS

In this chapter the models for stress-strain relationship and strength will be applied to some of the typical results of the calculation mentioned in the previous chapter.

4.1 Fuel Block

Fuel block is considered to be a hexagonal graphite block 334 mm in the distance between the opposite side planes, 700 mm in height which has 15 vertical holes 56 mm in diameter. To make application of the model as simple as possible, the block was approximated to be 15 hollow tubes each of which has an inner diameter of 56 mm. It was also approximated that summation of the cross-section of each tube is to be equal to that of the fuel block. This approximation resulted in 15 tubes 90.6 mm in outer diameter and 56 mm in inner diameter.

Since, among the results shown in Chapter III, that for 1273 K in use of L-H equation seemed to be the most severe case, stress-strain relationship and strength of the fuel block in this case is estimated here using the equations shown in Chapter II.

The above approximation and the result shown in Fig.17(c) make it possible to draw a schematic shown in Fig.24 for a unit hollow tube. Here, burn-off levels less than 0.1 % were neglected. Modifying Eqn.(3) we obtain

the cases of the first order and Langmuir-Hinshelwood equations, respectively.

(2) Core support post

Burn-off profiles of the core support post calculated at 1273K and 1373L are shown in Figs.20 through 23, where Figs.20 and 21 are the results obtained in use of the first order equation, and the Langmuir-Hinshelwood equation was used in Figs.22 and 23.

4. APPLICATION OF THE STRENGTH LOSS MODEL TO
THE OXIDIZED COMPONENTS

In this chapter the models for stress-strain relationship and strength will be applied to some of the typical results of the calculation mentioned in the previous chapter.

4.1 Fuel Block

Fuel block is considered to be a hexagonal graphite block 334 mm in the distance between the opposite side planes, 700 mm in height which has 15 vertical holes 56 mm in diameter. To make application of the model as simple as possible, the block was approximated to be 15 hollow tubes each of which has an inner diameter of 56 mm. It was also approximated that summation of the cross-section of each tube is to be equal to that of the fuel block. This approximation resulted in 15 tubes 90.6 mm in outer diameter and 56 mm in inner diameter.

Since, among the results shown in Chapter III, that for 1273 K in use of L-H equation seemed to be the most severe case, stress-strain relationship and strength of the fuel block in this case is estimated here using the equations shown in Chapter II.

The above approximation and the result shown in Fig.17(c) make it possible to draw a schematic shown in Fig.24 for a unit hollow tube. Here, burn-off levels less than 0.1 % were neglected. Modifying Eqn.(3) we obtain

$$P = \int_{r_i}^{r_s} \sigma 2\pi r \, dr = \int_{r_i}^{r_1} \sigma 2\pi r \, dr + \pi(r_2^2 - r_1^2) \, \sigma_0(\epsilon) + \int_{r_2}^{r_s} \sigma 2\pi r \, dr \qquad (60)$$

Here, r_i : inner radius, $\quad r_s$: outer radius,

$\quad r_1$: inner cut-off radius, $\quad r_2$: outer cut-off radius.

The integrals in the right side of Eqn.(60) can be obtained in a way similar to that in Eqn.(3). Taking $P/\pi(r_s^2 - r_i^2) = \sigma(\epsilon)$, we obtain

$\sigma(\epsilon)/\sigma_0(\epsilon) = 0.937$.

Compressive strength of the hollow tube was estimated following the idea described in Chapter II. We assume that fracture would initiate at both inner and outer surfaces and the length of fractured portions is always the same for the outer and inner. Based on this assumption we obtain, for load,

$$P(r) = \pi(r_1^2 - r^2)(\rho/\rho_0)^n \, \sigma_{f0} + \pi(r_2^2 - r_1^2) \, \sigma_{f0}$$

$$+ \pi[(r_s + r_i - r)^2 - r_2^2] \, (\rho/\rho_0)^n \, \sigma_{f0} \qquad (61)$$

Thus, σ_f is to be estimated finding the maximum of $P(r)$ in terms of r. From Eqn.(61),

$$\frac{\sigma_f(r)}{\sigma_{f0}} = \frac{1}{r_s^2 - r_i^2} \, [\,(r_1^2 - r^2)(\frac{\rho}{\rho_0})^n + (r^2 - r^2) + \{(r_s + r_1 - r)^2$$

$$- r_2^2 \} \, (\frac{\rho}{\rho_0})^n \,] \qquad (62)$$

The calculation to find the maximum of the right side of the above equation was done numerically, giving rise to a value of $\sigma_f / \sigma_{f0} = 0.968$.

4.2 Core Support Post

For the same reason as that for 4.1, we deal with the burn-off profile shown in Fig.21. Let the diameter of the post 150 mm. Burn-off is assumed to be the same along the longitudinal axis. Fig.25 shows a schematic of the profile in this case. Modifying Eqn.(3) we obtain

$$P = \pi r_1^2 \, \sigma_0(\epsilon) + \int_{r1}^{r'_s} 2\pi r \, \sigma(\epsilon) \, dr \tag{63}$$

Here, r'_s is the difference between the original radius and the thickness of the surface layer removed because of erosion, i.e.,

$$r'_s = 75 - 0.3 \text{ mm}.$$

From Eqn.(63),

$$\sigma(\epsilon) = (\frac{r_1}{r_s})^2 \, \sigma_0(\epsilon) + \sigma_0(\epsilon) \, \rho_0^{-4.6} \int_{1.580}^{1.748} f(\rho) f'(\rho) \, d\rho \tag{64}$$

The right side of Eqn.(63) was calculated numerically, giving rise to a value of $\sigma(\epsilon)/\sigma_0(\epsilon) = 0.967$. Since a layer 0.3 mm in thickness was removed from the surface, the nominal change in stress-strain relationship is supposed to be $\sigma(\epsilon)/\sigma_0(\epsilon) = 0.967 \times (74.7/75.0)^2 = 0.959$. This implies about 4 % decrease in stress at a give strain, ϵ.

Compressive strength of the post is estimated finding the maximum of the following equation.

$$P(r) = \pi r_1^2 \, \sigma_{f0} + \pi(r^2 - r_1^2) \, \sigma_{f0} \, (\frac{\rho}{\rho_0})^n \tag{65}$$

$$\sigma_f(r) = \frac{P(r)}{r_s^2} \tag{66}$$

The maximum of the right side of Eqn.(66) was obtained numerically using the burn-off profile shown in Fig.25. As a result we obtain $\sigma_f/\sigma_{f0} = 0.974$. This means that the strength loss of core support post after its service life would be less than 3 %.

ACKNOWLEDGEMENTS

$$P = \pi r_1^2 \, \sigma_0(\varepsilon) + \int_{r1}^{r'_s} 2\pi r \, \sigma(\varepsilon) \, dr \qquad (63)$$

Here, r'_s is the difference between the original radius and the thickness of the surface layer removed because of erosion, i.e.,

$$r'_s = 75 - 0.3 \text{ mm}.$$

From Eqn.(63),

$$\sigma(\varepsilon) = \left(\frac{r_1}{r_s}\right)^2 \sigma_0(\varepsilon) + \sigma_0(\varepsilon) \, \rho_0^{-4.6} \int_{1.580}^{1.748} f(\rho)f'(\rho) \, d\rho \qquad (64)$$

The right side of Eqn.(63) was calculated numerically, giving rise to a value of $\sigma(\varepsilon)/\sigma_0(\varepsilon) = 0.967$. Since a layer 0.3 mm in thickness was removed from the surface, the nominal change in stress-strain relationship is supposed to be $\sigma(\varepsilon)/\sigma_0(\varepsilon) = 0.967 \times (74.7/75.0)^2 = 0.959$. This implies about 4 % decrease in stress at a give strain, ε.

Compressive strength of the post is estimated finding the maximum of the following equation.

$$P(r) = \pi r_1^2 \, \sigma_{f0} + \pi(r^2 - r_1^2) \, \sigma_{f0} \left(\frac{\rho}{\rho_0}\right)^n \qquad (65)$$

$$\sigma_f(r) = \frac{P(r)}{r_s^2} \qquad (66)$$

The maximum of the right side of Eqn.(66) was obtained numerically using the burn-off profile shown in Fig.25. As a result we obtain $\sigma_f/\sigma_{f0} = 0.974$. This means that the strength loss of core support post after its service life would be less than 3 %.

ACKNOWLEDGEMENTS

REFERENCES

1) M.B. Peroomian et al, GA-A 12493 (1974).

2) R.J. Price, GA-A 13524 (1975).

3) M. Eto and F.B. Growcock, BNL-NUREG-51493 (1981).

4) M. Eto and F.B. Growcock, Carbon 21, 135 (1983).

5) M. Eto et al, Intn'l Carbon Conf., Baden-Baden, Extended Abstracts, p.582 (1986).

6) S. Nomura et al, to be published.

7) M. Eto et al, 16th Biennial Conf. on Carbon, San Diego, Extended Abstracts, p.566(1983).

8) S. Yoda et al, Intn'l Carbon Conf., Bordeaux, Extended Abstracts, p.444 (1984).

9) S. Yoda et al, Carbon 23, 33 (1985).

10) S. Yoda et al, 17th Biennial Conf. on Carbon, Kentucky, Extended Abstracts, p.285 (1984).

11) C. Velasquez et al, GA-A 15799 (1978).

12) H. Imai et al, 6th Annual Meeting of Carbon Society of Japan.

13) P.L. Walker, Jr. et al, Advances in Catalysis 11, 133 (1959).

14) M. Everett et al, Chemistry and Physics of Carbon, vol.3, (ed. P.L. Walker, Jr.), Marcel Dekker, New York, pp.289-436, (1968).

15) M.B. Peroomian et al, GA-A 12493 (1974).

16) P.L. Walker, Jr. et al, Advances in Catalysis 11, 133 (1959)

17) R. Burnette et al, GA-A 15799 (1980).

18) H. Imai et al, JAERI-M 8848 (1980).

19) H. Imai et al, JAERI-M 9166 (1980).

20) K. Hayashi, private communication.

21) M.H. Dodson, DEG Report 148 (CA) (1960).

22) F.P.O. Ashworth et al, Proc. Intn'l Conf., BNES, p.30.1 (1973)

Table 1. Flow stress of unoxidized specimens under compressive stress and the ratios of the flow stresses of specimens oxidized to various burn-off levels to that of the unoxidized specimen at any strain, each ratio being almost constant irrespective of strain

Total Strain	VIRGIN ρ_o=1.76	0.9% B. O.		3.8% B. O.		6.0% B. O.		9.6% B. O.		16.0% B. O.	
(%)	Stress(MPa) σ_o	Stress	σ/σ_o	Stress	σ/σ_o	Stress	σ/σ_o	Stress	σ/σ_o	Stress	σ/σ_o
0.25	16.67	14.09	0.88	12.28	0.74	11.83	0.71	10.83	0.65	8.90	0.53
0.50	29.38	26.11	0.89	22.20	0.76	21.02	0.71	18.75	0.64	15.53	0.53
0.75	39.45	33.89	0.86	30.18	0.76	28.26	0.71	25.07	0.64	20.39	0.52
1.00	47.58	40.83	0.86	36.53	0.77	34.07	0.71	29.86	0.63	24.43	0.51
1.25	53.99	46.44	0.86	41.64	0.77	38.56	0.71	33.73	0.63	27.63	0.51
1.50	59.27	51.04	0.86	45.84	0.77	42.23	0.71	37.00	0.63	30.12	0.51
1.75	63.44	54.81	0.86	49.32	0.78	45.19	0.71	39.85	0.63	32.08	0.51
2.00	66.90	58.08	0.87	52.18	0.78	47.74	0.71	42.40	0.64	33.74	0.50
2.25	69.95	60.73	0.87	54.64	0.78	49.88	0.71	44.40	0.64	35.29	0.51
2.50	72.59	63.28	0.87	56.79	0.78	51.72	0.71	46.47	0.64		
2.75	74.83	65.32	0.87	58.73	0.79	53.46	0.71	48.21	0.64		
3.00	76.86	67.16	0.87	60.34	0.78	54.68	0.71	49.53	0.64		
3.25	76.96	68.90	0.90	61.90	0.80	56.01	0.73				
3.50	80.32	70.43	0.88	63.34	0.79	56.59	0.71				
		Average	0.87		0.78		0.71		0.64		0.51

VARIOUS REACTION CONTROL REGIMES AS A FUNCTION OF TEMPERATURE RATURE
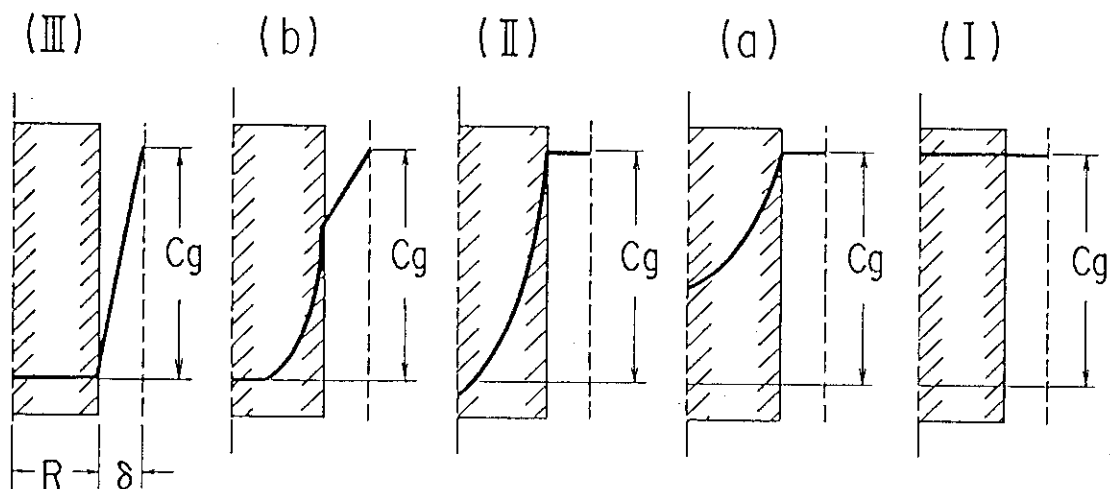
Cg : Concentration of reacting gas

R : Radius of cylindrical specimen

(I) : Chemical reaction control

(II) : In - pore diffusion control

(III) : Boundary layer diffusion control

Fig. 1 Schematic for various reaction control regimes as a function of temperature

Estimation of Oxidation of Graphite Components

Accelerated   Experiments
on Laboratory   Scale

$T = 1050 - 1350$ K

$C_{H_2O} = 0.65 - 1.8$ %

$P_{He} = 0.1$ MPa

< Extrapolation >

Normal operation

$T = 1200 - 1400$ K

$P_{H_2O} = 0.2$ vpm

$P_{He} = 4$ MPa

< Basic data >

Water ingress accident

$T = 1100 - 1400$ K

$P_{H_2O} = 0.23$ MPa

$P_{He} = 4.3$ MPa

Compensation   for
in- pile condition

Estimation   of
oxidation amount
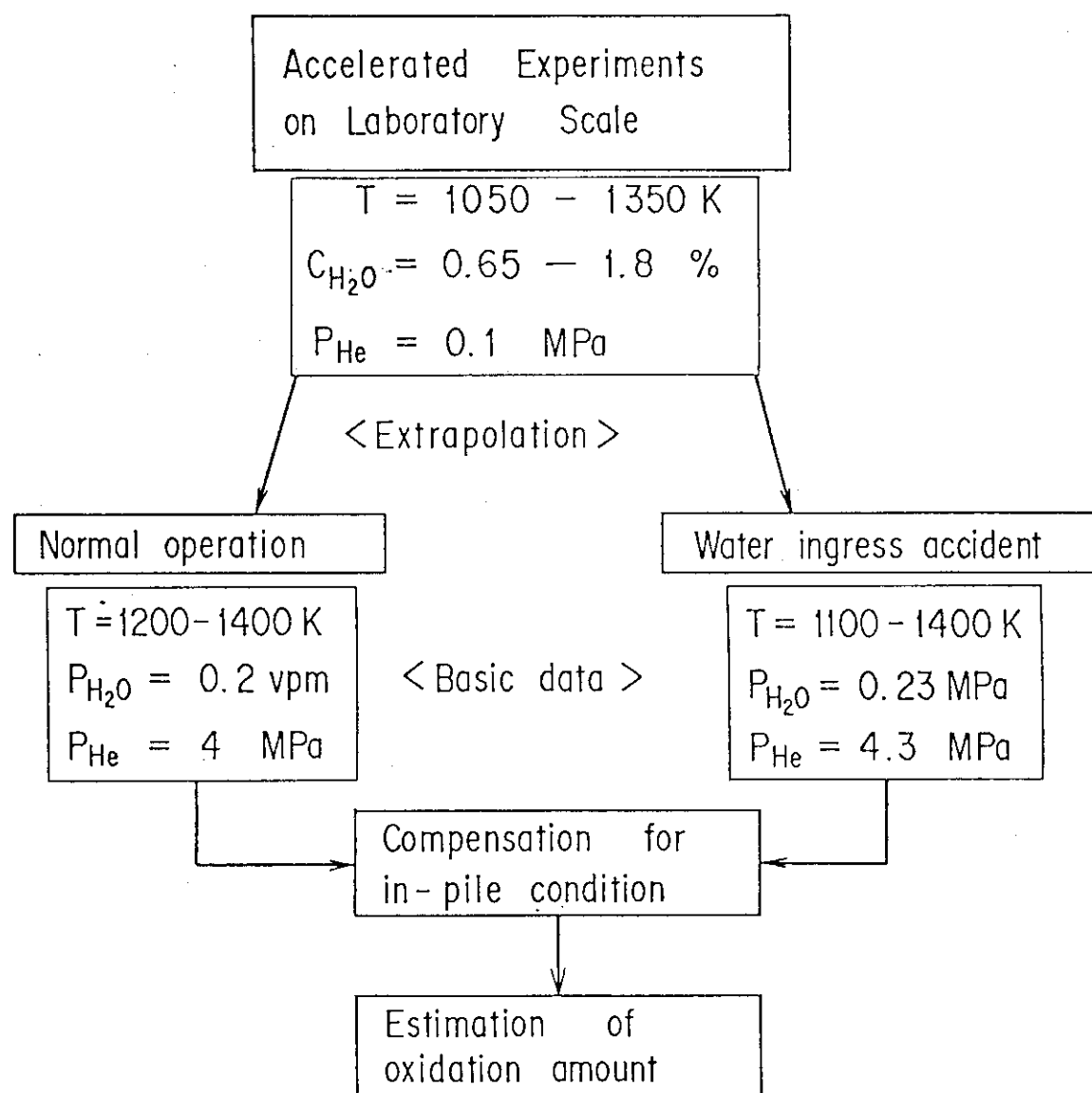
Fig. 2   Procedure for the estimation of oxidation of the
graphite components in the VHTR
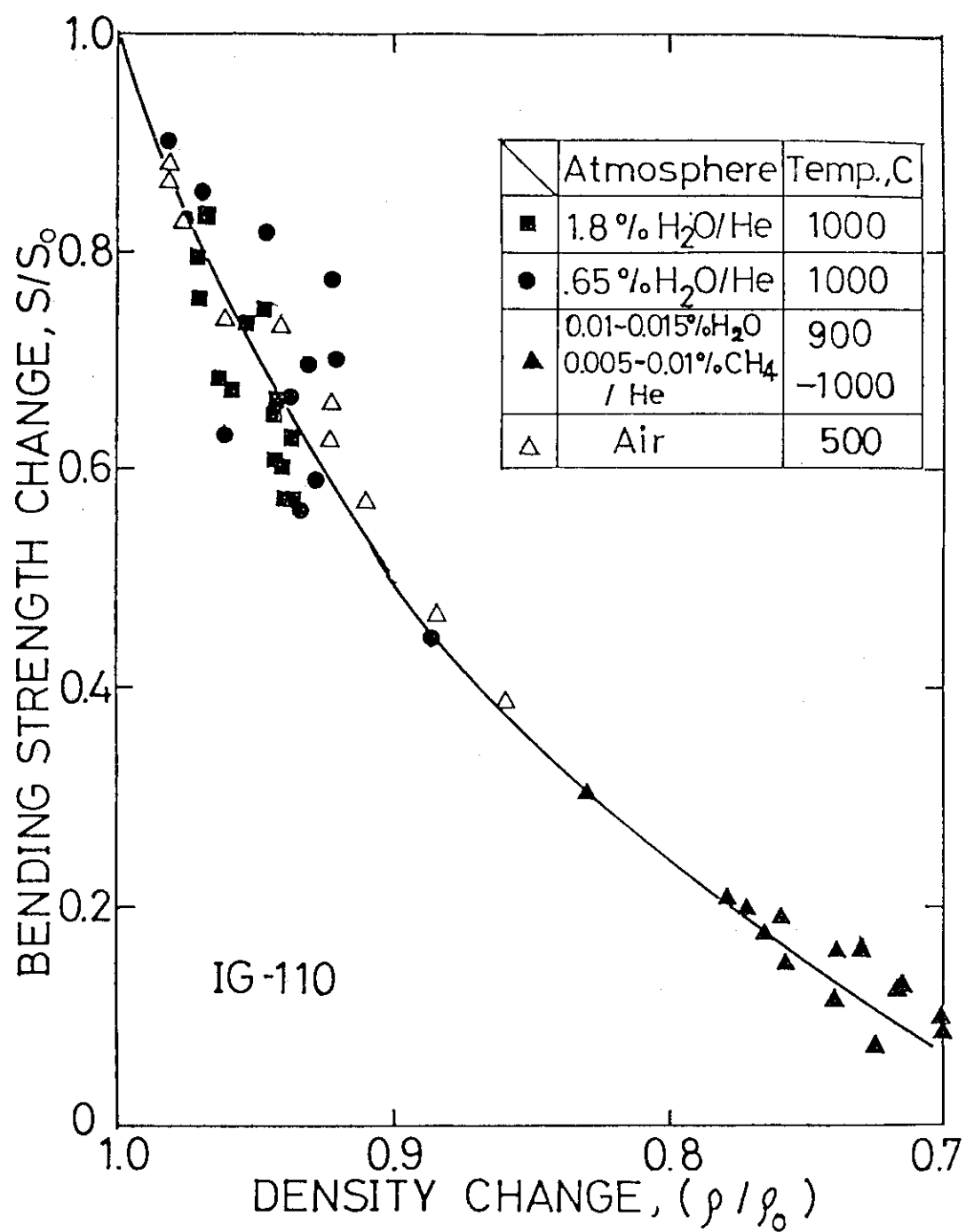
Fig. 3 Change in bending strength of IG-110 graphite oxidized in different conditions
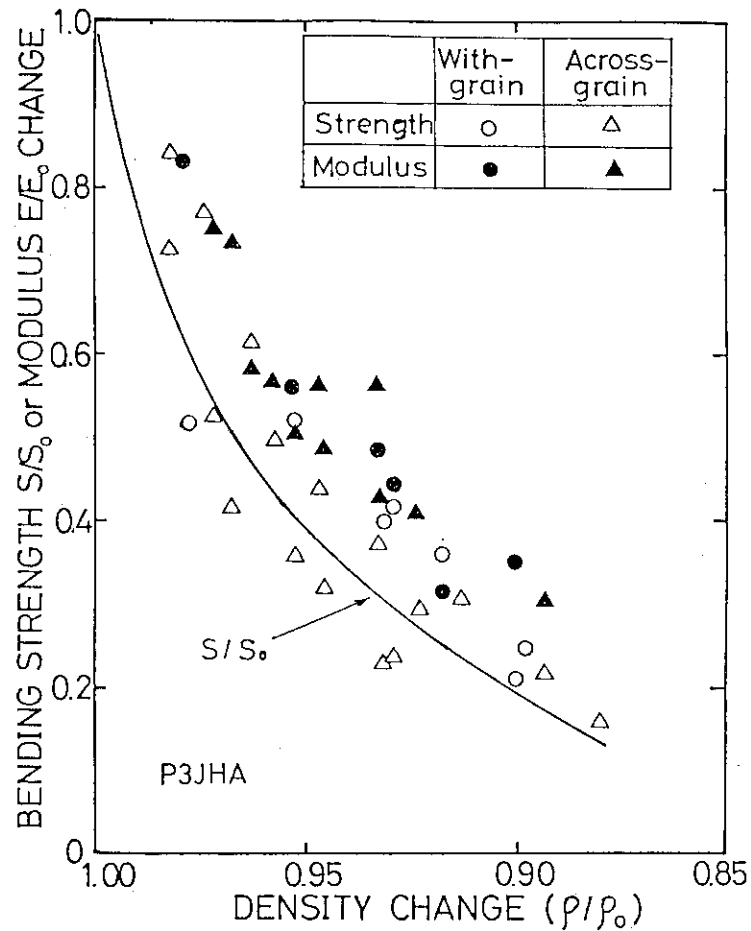
Fig. 4 Changes in bending strength and Young's modulus of P3JHA graphite oxidized at 773 K in air.
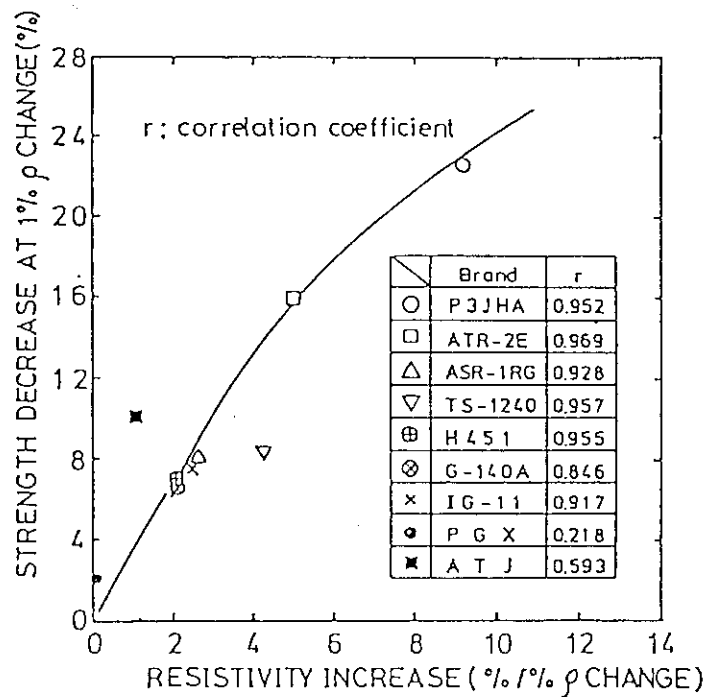
Fig. 5 Plots of the decrease in bending strength vs. resistivityincrease for various HTGR graphites
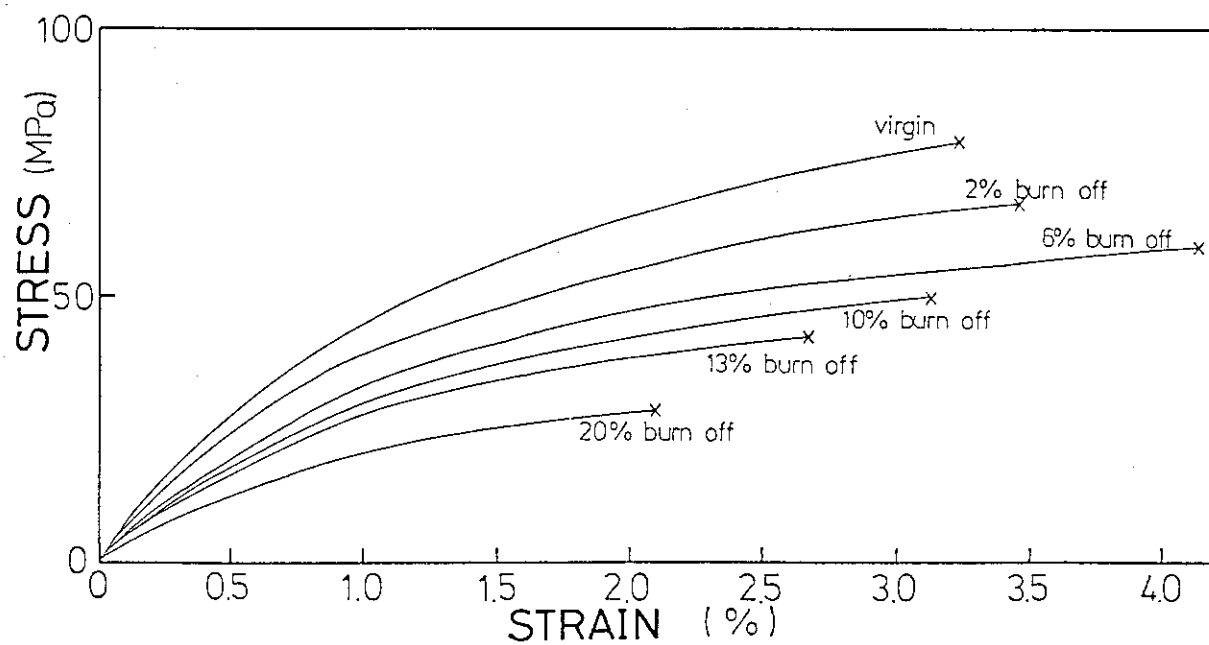
Fig. 6   Compressive stress-strain curves for specimens
         uniformly oxidized to different burn-off levels
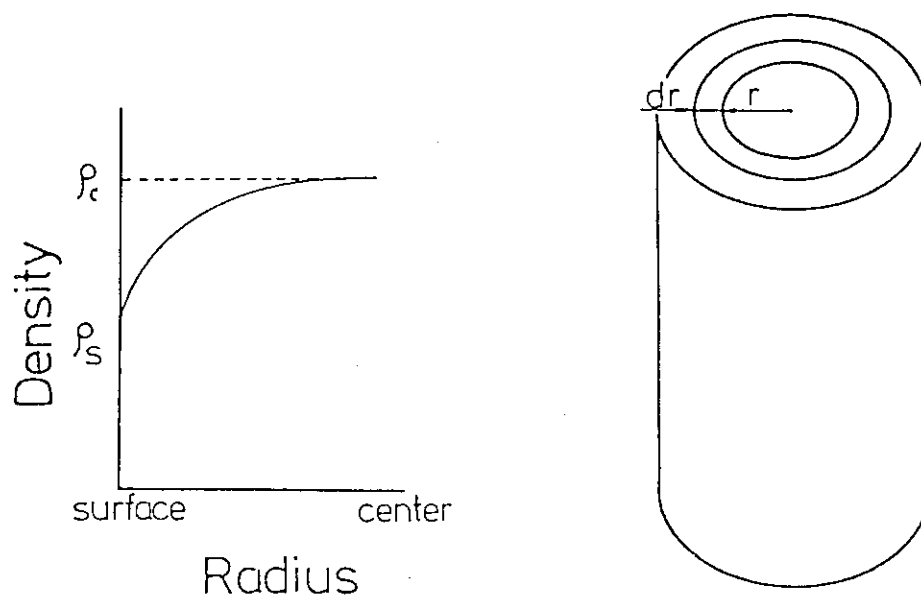
Fig. 7   Schematic for a cylindrical specimen with oxidation
         gradient in the radial direction
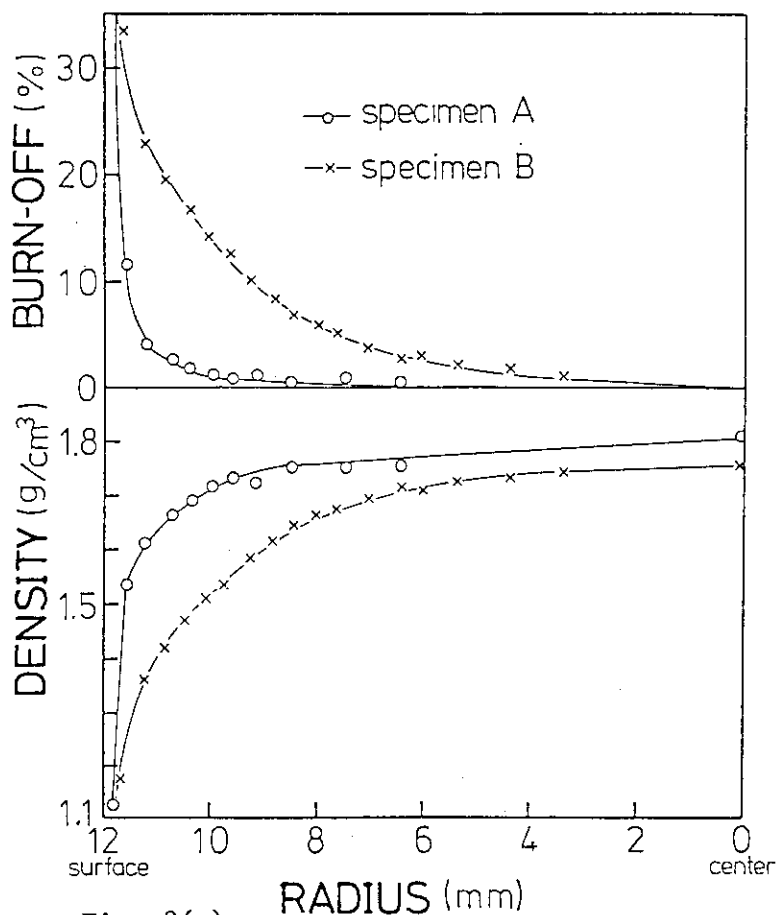
Fig. 8(a)
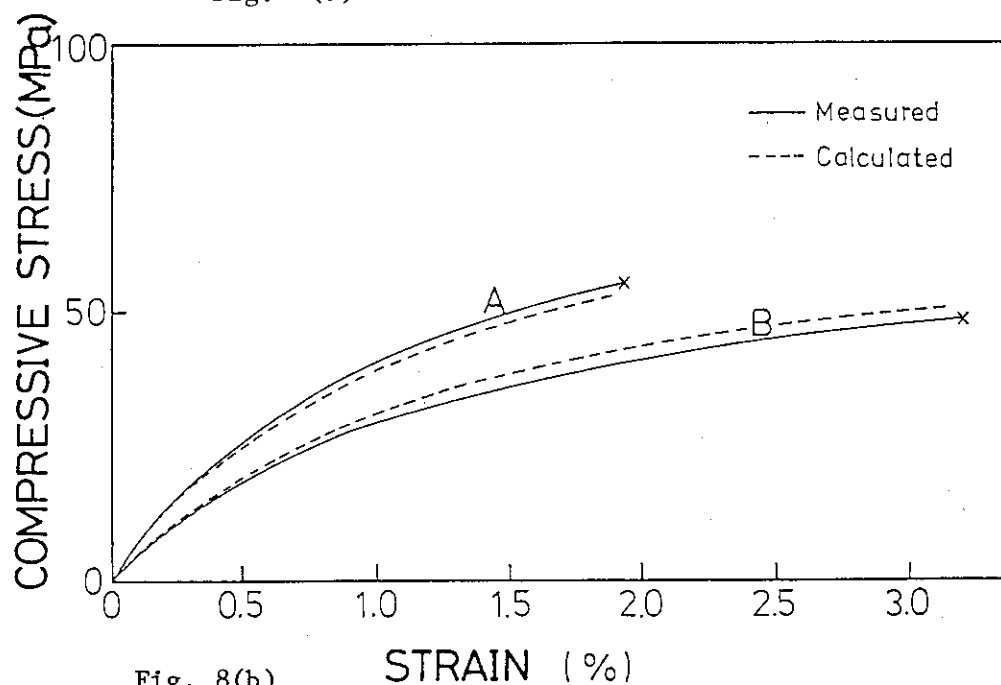
Fig. 8(b)

Fig. 8 (a) Local burn-off profile of specimens A and B with 4.75 and 11.75 %, respectively. (b) Compressive stress-strain curves for the specimens with oxidation gradients shown in (a). (c) Local burn-off profile of tensile specimens A and B with 4.60 and 9.68 %, respectively. (d) Tensile stress-strain curves for the specimens with oxidation gradient shown in (c).
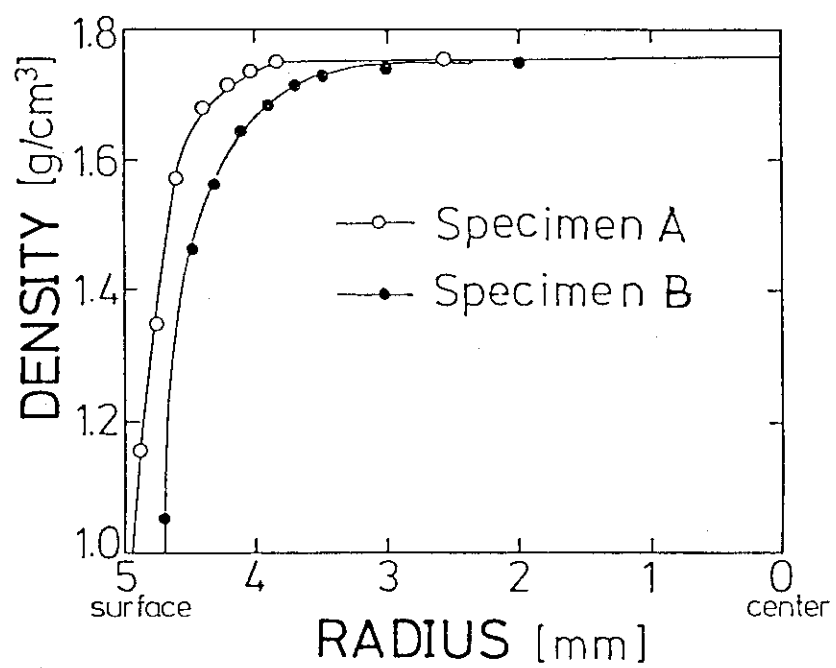
Fig. 8(c)
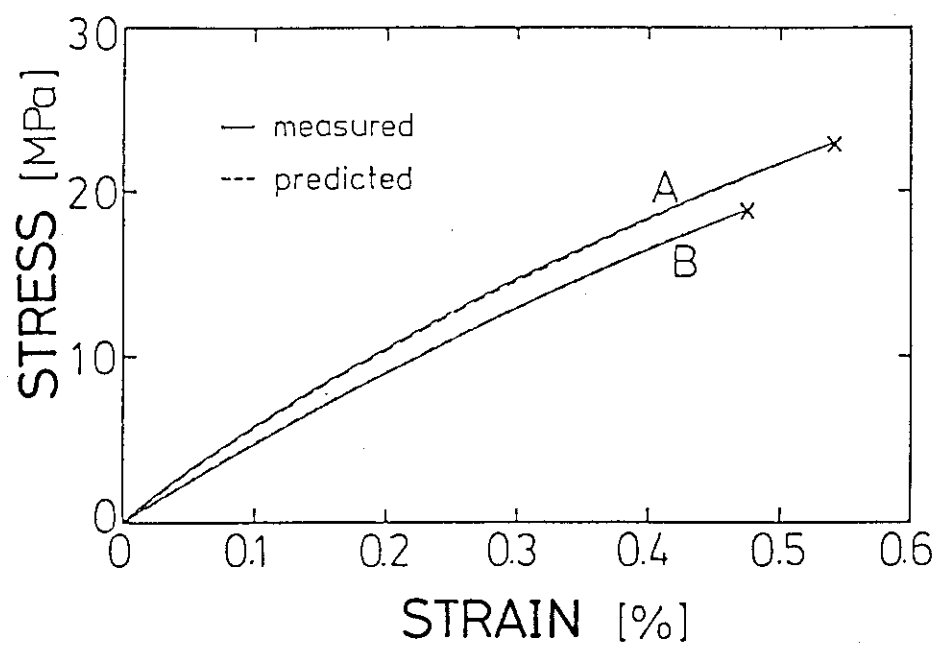
Fig. 8(d)
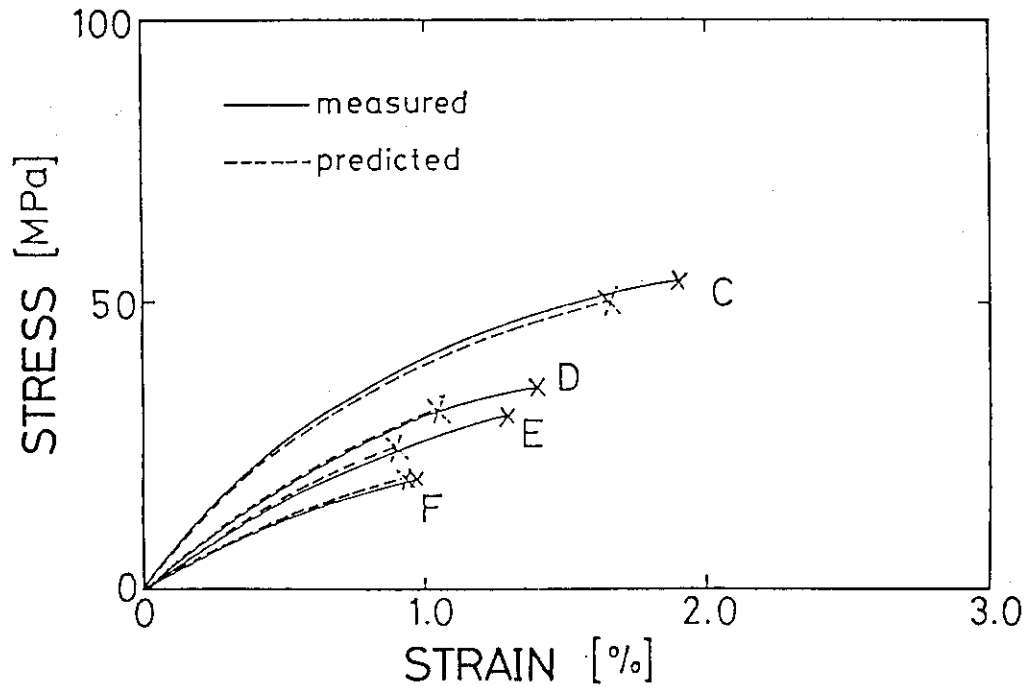
Fig. 9   Measured and predicted compresive strength together with
          stress-strain curves for several oxidized specimens
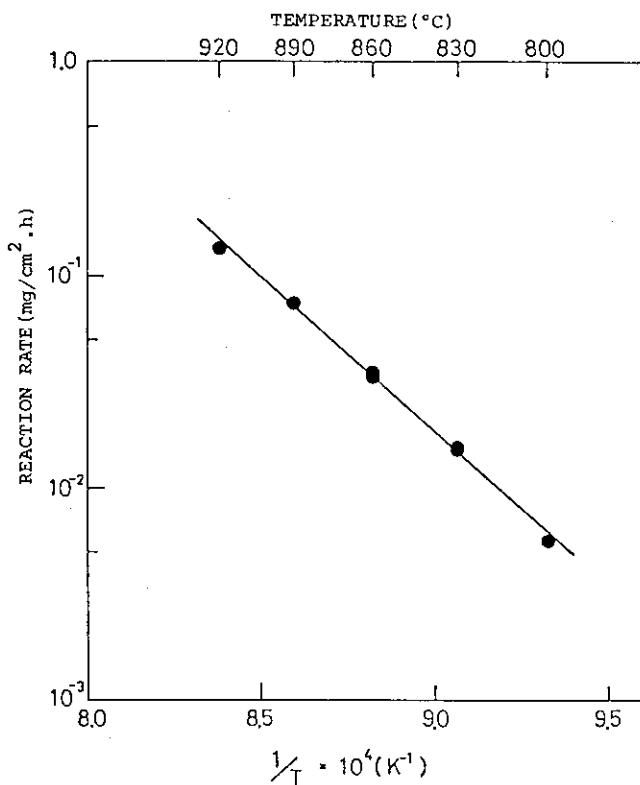
Fig. 10

Temperature dependence of reaction
rate of IG-110 gra-phite oxidized
in 0.65 % water vapor/helium mixture
at the atmospheric pressure
(burn-off: 3 mg/cm²)
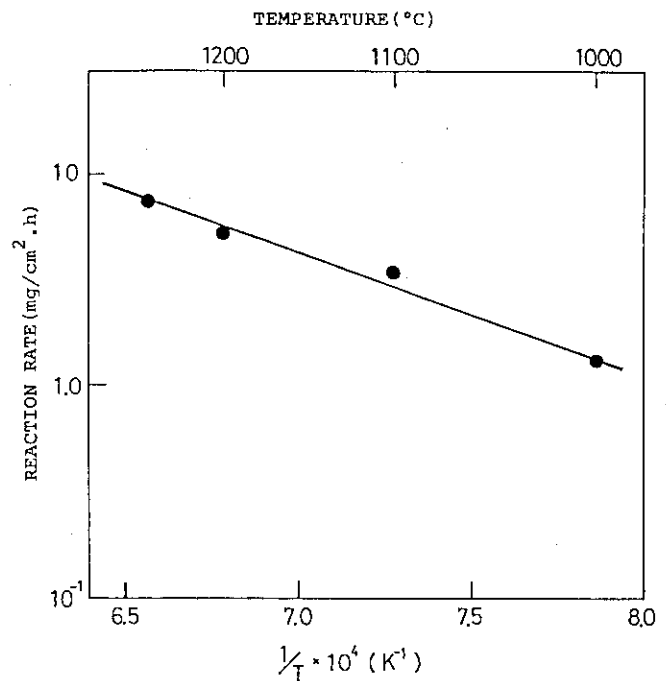
Fig. 11

Temperature dependence of reaction
rate of IG-110 gra-phite oxidized
in 0.65 % water vapor/helium mixture
at the atmospheric pressure
(burn-off: 40 mg/cm²)
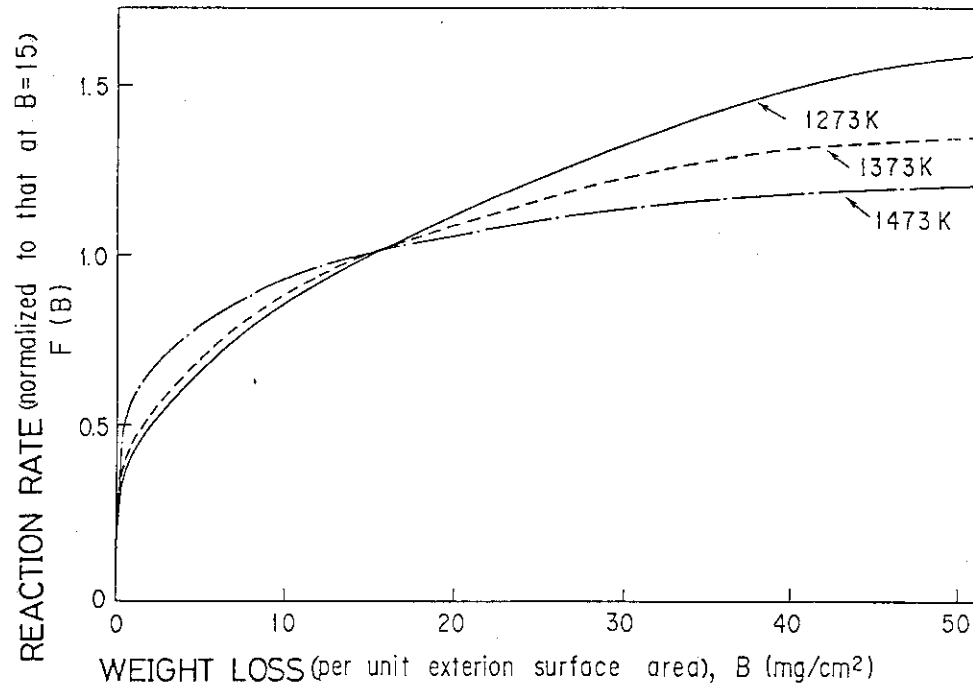
Fig. 12   Plots of reaction rate normalized to that B=15 vs.
weight loss per unit extension surface area, B
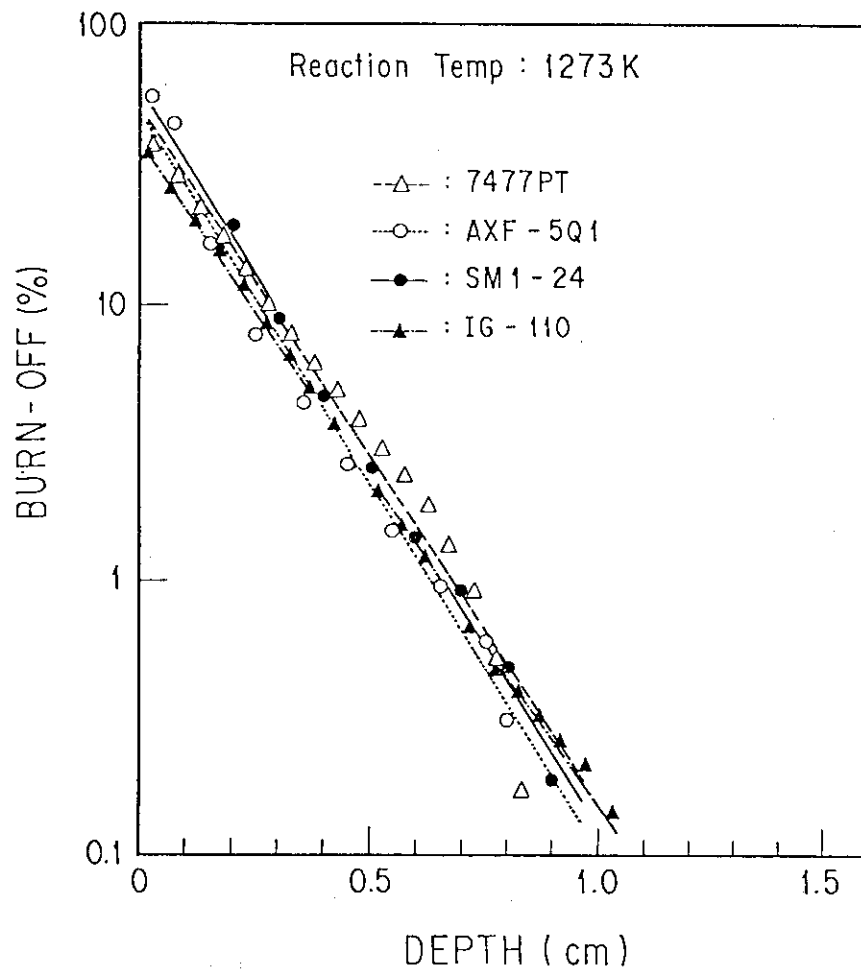
Fig. 13   Burn-off profiles of some HTGR graphites oxidized in
a water vapor/helium mixture
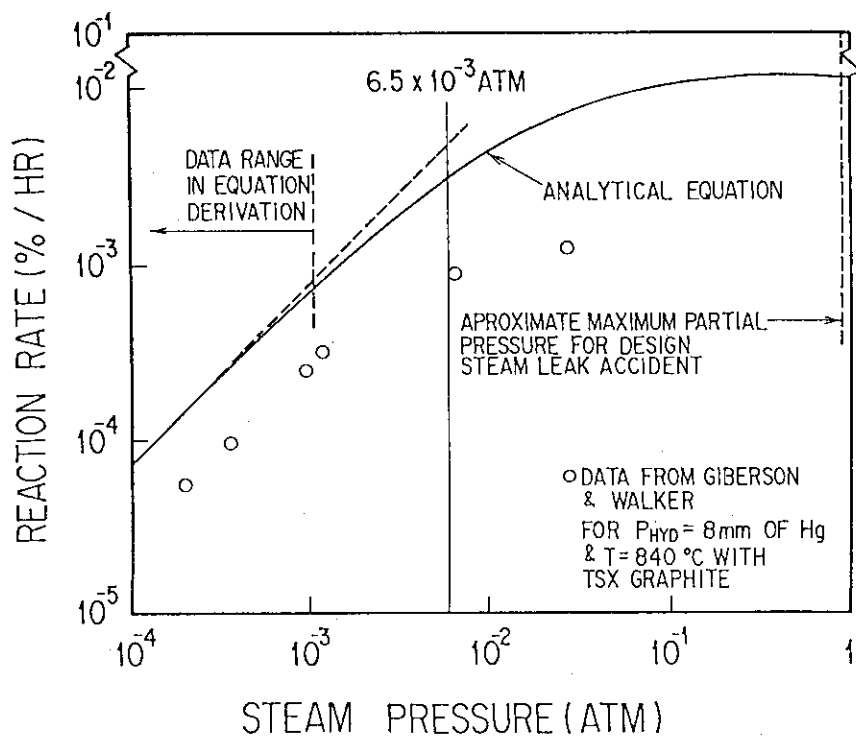
Fig. 14   Dependence of reaction rate on the partial pressure of
water vapor [5]
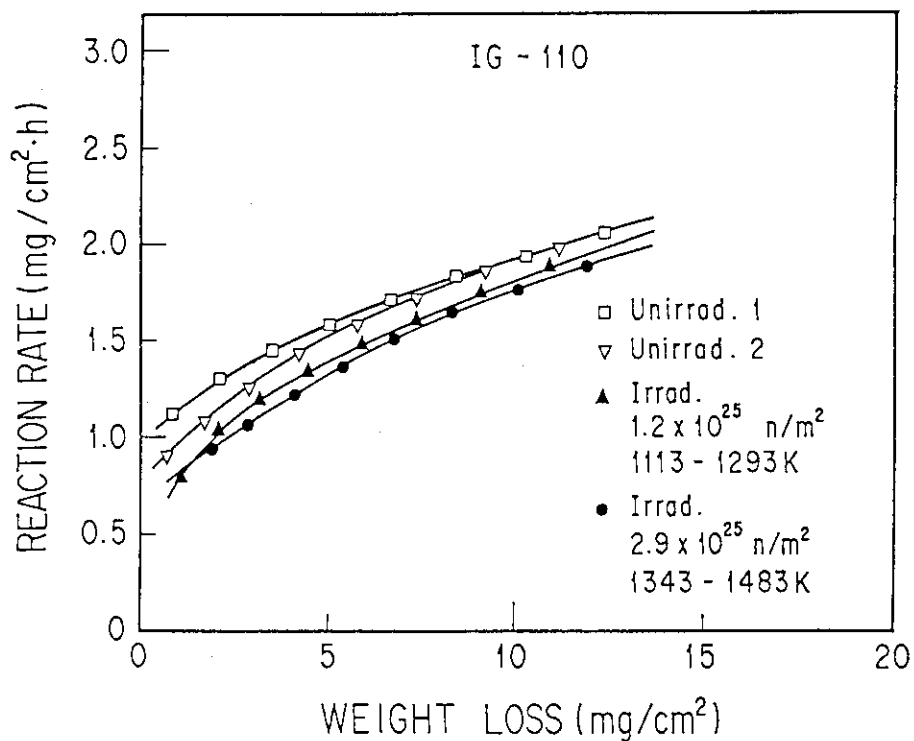
Fig. 15   Reaction rate of unirradiated or neutron-irradiated
IG-110 graphite oxidized with water vapor
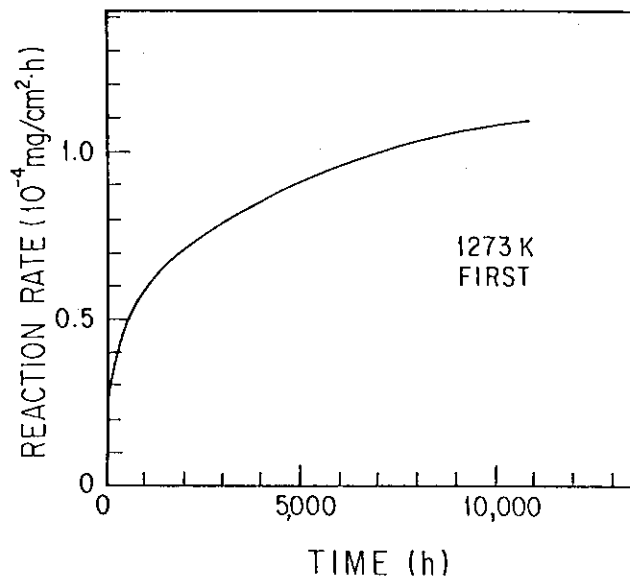
Fig. 16(a)
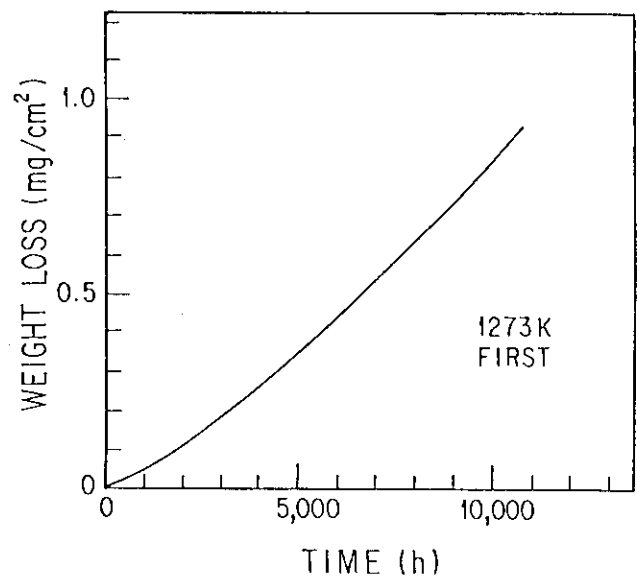
Fig. 16(b)
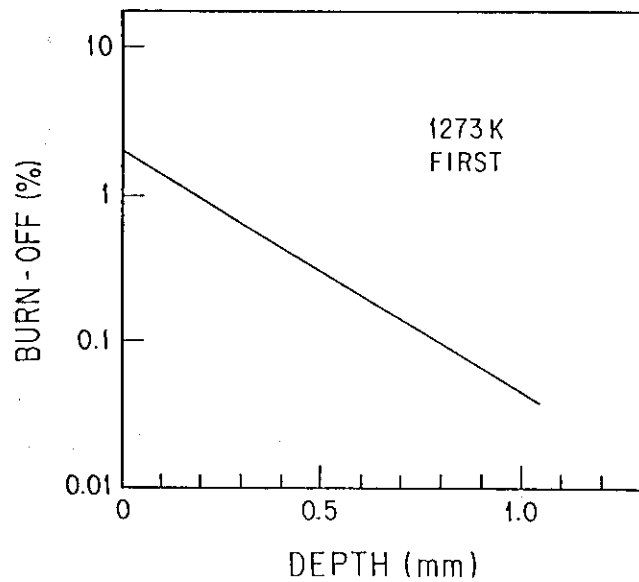
Fig. 16(c)

Fig. 16   Calculations of (a) reaction rate, (b) weight loss and
          (c) burn-off profile for the fuel block oxidized at
          1273 K in use of the first order equation
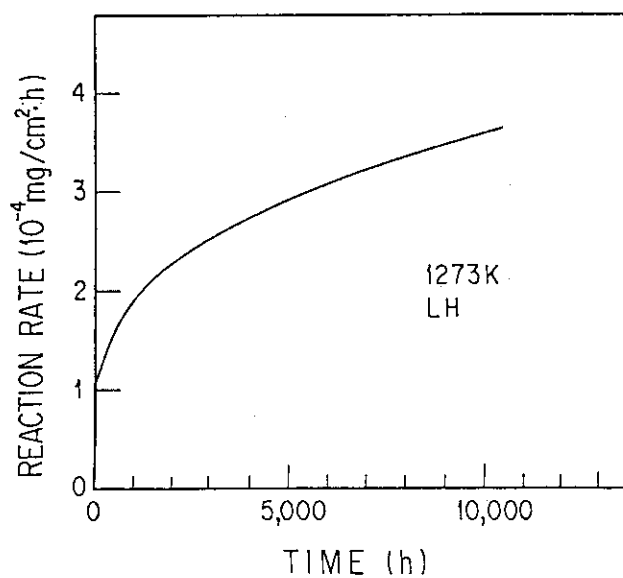
Fig. 17(a)
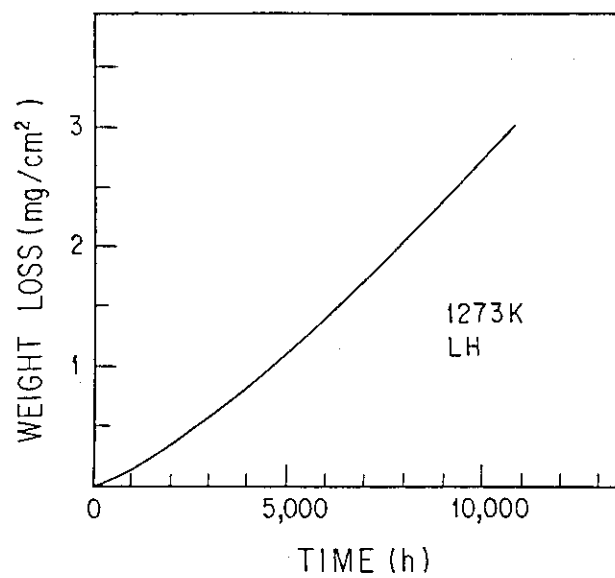
Fig. 17(b)
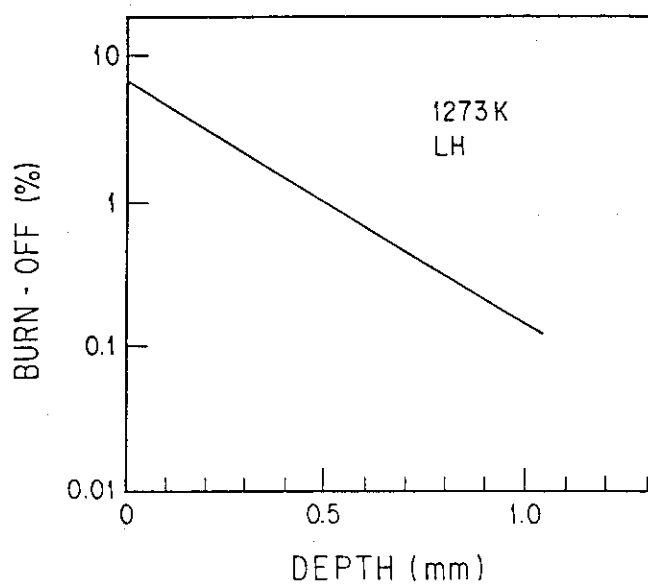
Fig. 17(c)

Fig. 17　Calculations of (a) reaction rate, (o) weight loss and
(c) burn-off profile for the fuel block oxidized at
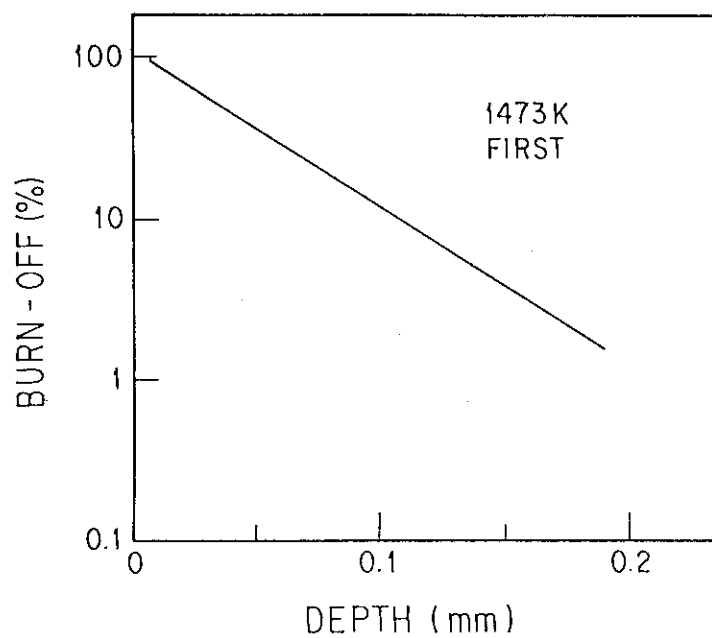1273 K in use of Langmuir-Hinshelwood equation

Fig. 18   Burn-off profile for the fuel block oxidized at 1473 K
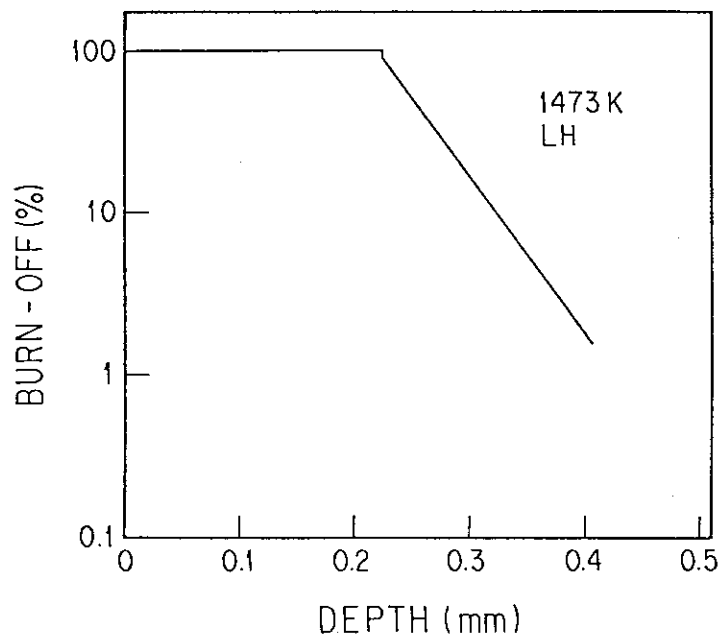in use of the first order equation

Fig. 19   Burn-off profile for the fuel block oxidized at 1473 K
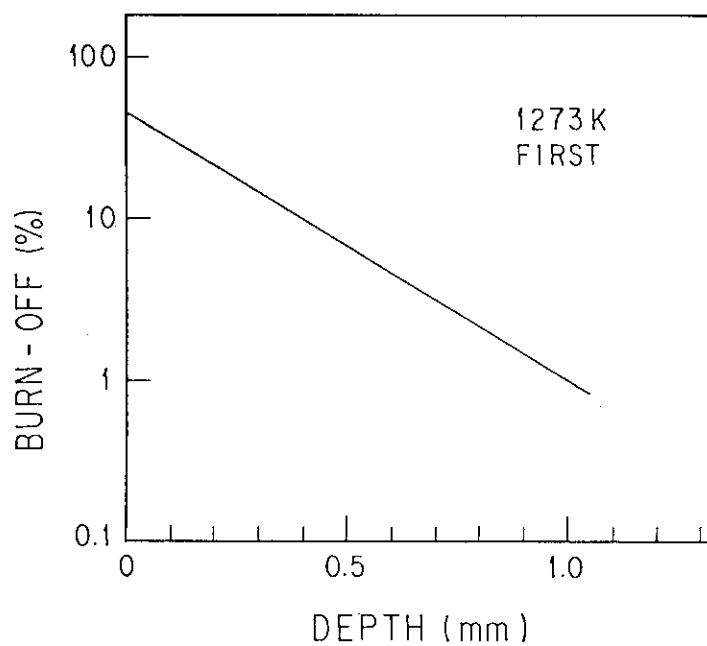in use of Langmuir-Hinshelwood equation

Fig. 20   Burn-off profile for the core support post oxidized at
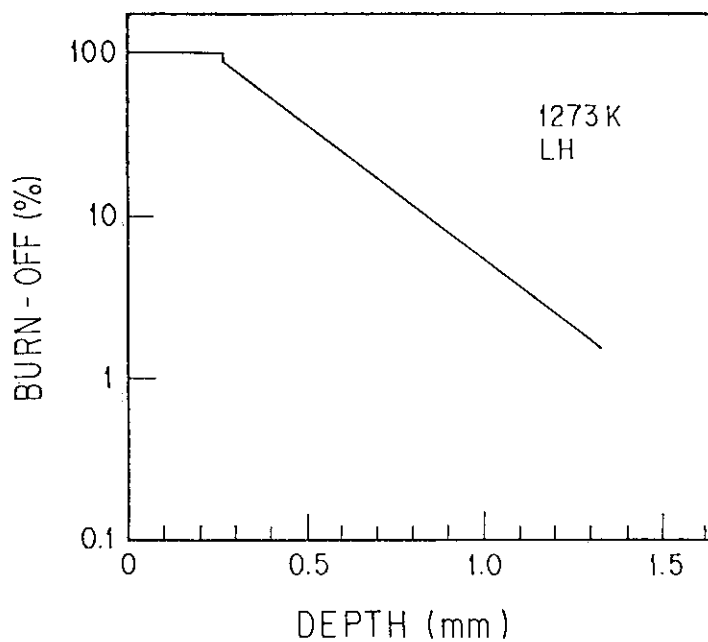1273 K in use of the first order equation

Fig. 21   Burn-off profile for the core support post oxidized at
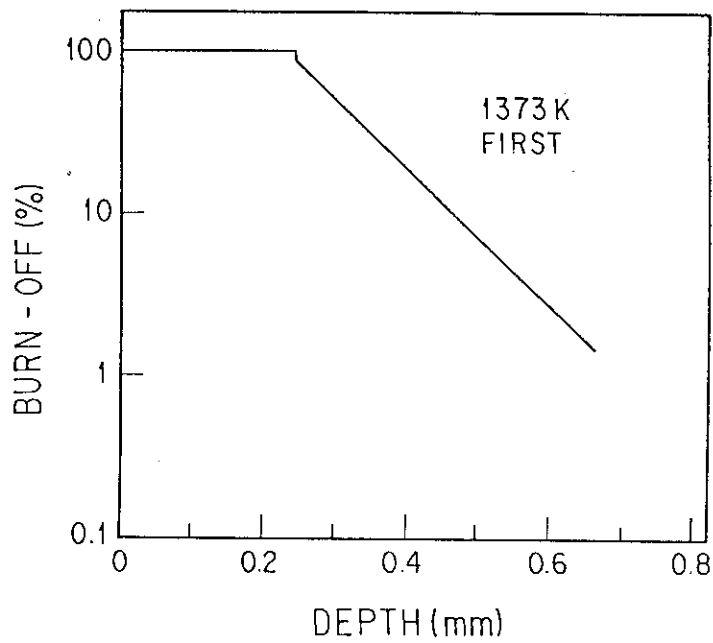1273 K in use of the Langmuir-Hinshelwood equation

Fig. 22   Burn-off profile for the core support post oxidized at
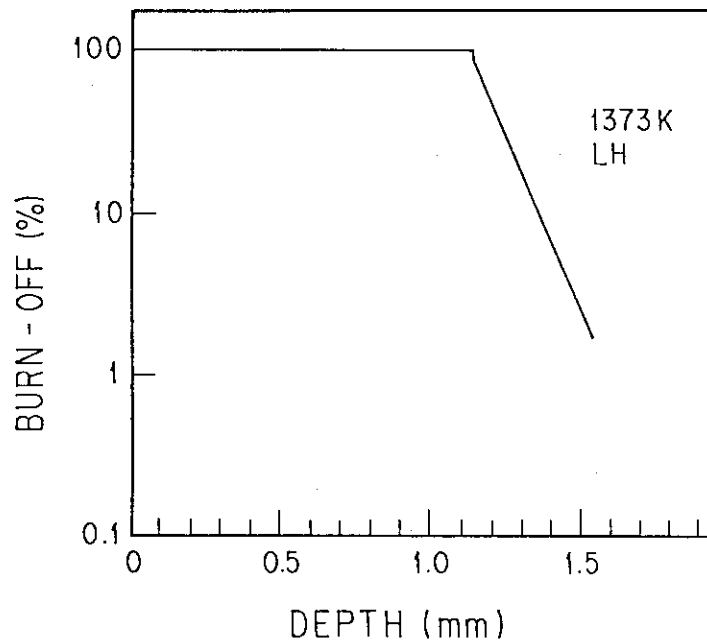1373 K in use of the first order equation

Fig. 23   Burn-off profile for the core support post oxidized at
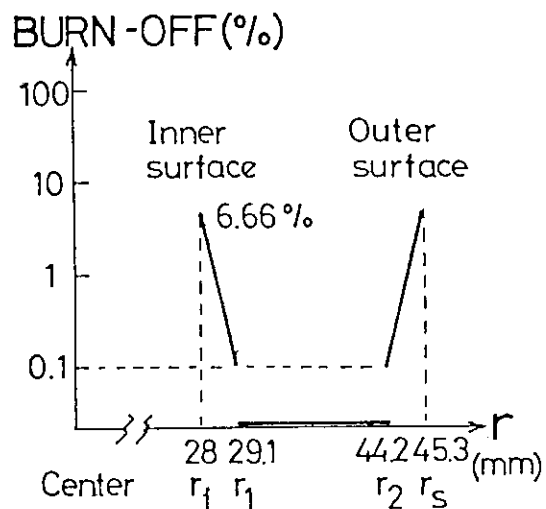1373 K in use of Langmuir-Hinshelwood equation

Fig. 24   Schematic for the calculation of the stress-strain characteristics of a oxidized hollow tube which is an approximation for fuel block
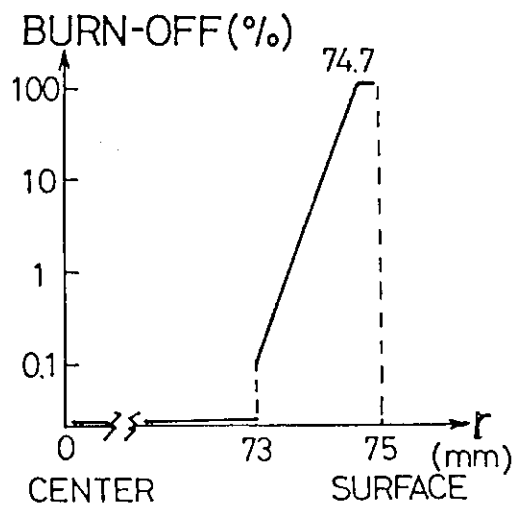

Fig. 25   Schematic for the calculation of the stress-starain characteristics of the oxidized core support post

APPENDIX 1

Application of Langmuir-Hinshelwood equation to calculation
of rate in the in-pore diffusion control regime

Oxidation of nuclear graphites with water-vapor is controlled simulta-
neously by diffusion of water-vapor in the pores of graphite and chemical
reaction on the pore walls. The diffusive flux of water-vapor was that
due primarily to the molecular diffusion at and above atmospheric pressure.
Most of the interior surface are not readily accessible to gas. There are
two limiting cases for the rate of the graphite corrosion. At lower
temperature with less reactive graphite, the oxidation rate is restricted
by the chemical reaction rate on the pore walls. At higher temperature
with more reactive graphite, the rate is controlled by the diffusive flux
of water-vapor in the pores. The in-pore diffusion controlled reaction is
confined to the the pore mouth area at the exterior surface of graphite.

In the mathmatical formulation, the followings were assumed for
simplifying the analysis.
(1) The interior surface area remains essentially unchanged during
    oxidation.
(2) The effective diffusivity De remains unchaged during oxidation.
(3) A possible contribution of the Knudsen diffusion in the diffusive
    flux is neglected.
(4) A possible effect of counter convective flux of product gases in the
    pores which is formed by volume increase in the reaction (7) is
    neglected.

2.1 Semi-infinite block

The oxidation reaction on the pore wall is

$$H_2O(g) + C(gr) = H_2(g) + CO(g) \tag{1}$$

Under steady state conditions, the local rate of oxidation R_ℓ is given by
the diffusive flux of water-vapor, J_{H_2O}

$$R_\ell = \text{div } J_{H_2O} \tag{2}$$

From Fick's law, the diffusive flux of water-vapor is

$$J_{H_2O} = \frac{D_e}{RT} \text{ grad } P_{H_2O} \qquad (3)$$

where grad P_{H_2O} represents the partial pressure gradient within the pores at any distance from the exterior surface. When the Langmuir-Hinshelwood equation is assumed for chemical reaction, the local chemical reaction within the graphite is given by

$$R_\ell (\text{g-mol } C \cdot cm^{-3} \cdot sec^{-1}) = \frac{K_1 \ P_{H_2O}}{1 + K_3 \ P_{H_2O}} \qquad (4)$$

An inhibition effect of hydrogen on the rate was neglected for simplicity because an observed rate to attain the steady state under inhibition effect is very slow[a].

In the present derivation J_{H_2O} is in g-mole H_2O/cm^3-sec, and the rate parameters K_1 and K_3 are in g-mole C/atm-cm^3-sec and in atm^{-1} respectively.

Combinations of equations (2), (3) and (4) give the following general differential equation for dual controlled oxidation of graphite under isothermal conditions

$$\text{div(grad } u) = \frac{R \ T}{D_e \ P} \cdot \frac{K_1}{K_3} \cdot \frac{u}{a+u} \qquad (5)$$

where P is total pressure of the system and u and a are dimensionless parameters defined as follows

$$u = P_{H_2O} / P_T , \qquad a = 1/(K_3 \ R_T) \qquad (6)$$

For the chemical reaction controlled zone, the gradient of u is nearly zero throughout the graphite body and the integrated rate Ro in unit volume of the graphite is R_ℓ. From equation (3), the other limiting case of in-pore diffusion controlled rate Rd in unit geometrical surface of the graphite is given by

$$Rd(\text{g-mol } C \cdot cm^{-2} \ sec^{-1}) = (J_{H_2O})_s = \frac{D_e \ T}{RT} (\text{grad } u)_s \qquad (7)$$

The subscript s denotes values of J_{H_2O} and grad u at the graphite exterior surface.

(a) C. Velasquaz, G. Hightower and R. Burnette, GA-A 14951 (1978)

For the unidimensional case of a semi-infinite block (an infinite mass in contact with gas at a plane surface $x = 0$), equations (5) and (7) become

$$\frac{d^2u}{dx^2} = \frac{RT}{D_e\,P} \cdot \frac{K_1}{K_3} \cdot \frac{u}{a+u} \tag{8}$$

$$Rd = \frac{D_e\,P}{RT} \left(\frac{du}{dx}\right)_s \tag{9}$$

Equation (8) can be integrated analytically from $x = 0$ to $x = \infty$ for the boundary conditions $du/dx = 0$ ($x = \infty$) and $u(x = 0) = u_s$ and Rd becomes

$$Rd = (P_{H_2O})_o \sqrt{\frac{D_eK_1}{RT}} \cdot \sqrt{\frac{2}{K_3(P_{H_2O})_o}\left[1 - \frac{1}{K_3(P_{H_2O})_o}\ln(1+K_3(P_{H_2O})_o\right]} \tag{10}$$

where $(P_{H_2O})_o$ is water-vapor partial pressure in the exterior gas phase and x is the distance from the exterior surface of the graphite.

If the graphite oxidation rate Rd represents Rd(1) for the laboratory condition($(P_{H_2O})_o = 6.5 \times 10^{-3}$ atm, $P = 1$ atm, $T = 1273K$) and Rd(2) for different condition with the same temperature, Rd(2) is given by

$$Rd(2) = \frac{Y(2)}{Y(1)} \cdot Rd(2) \tag{11}$$

$$Y = \sqrt{\frac{1}{P}\{(P_{H_2O})_o - \frac{1}{K_3}\ln\,(1+K_3(P_{H_2O})_o)\}} \tag{12}$$

where Y(1) and Y(2) are Y for the laboratory condition and for different condition with the same temperature, respectively.
In this derivation, $D_e \cdot P$ is assumed to be constant.

APPENDIX 2

The Flow Diagram of the Program for Calculation

The flow diagram of the program is shown in Fig.A.1. The program consists of four main parts: 1. Specifications of materials, 2. Calculation of $R_{p,ref}$, reaction rate at B=15 in the in-pile condition, 3. Calculation of reaction rate and weight loss as a function of time, 4. Calculation of burn-off profile. Each part consists of several sub-parts. The program will be explained below following the diagram.

1. Specifications of materials

Graphite or carbonaceous materials, IG-110, PGX and ASR-ORB are the candidates for VHTR use. Bulk density and other properties are determined according to appropriate references. Ratio of burn-off values to B are calculated from density and the exterior-surface-area-to-volume ratio on the assumption that the overall exterior surface is exposed to the same oxidizing temperature.

2. Calculation of $R_{p,ref}$

$R_{p,ref}$, reaction rate at a given burn-off B is calculated using the first order or Langmuir-Hinshelwood equations. Prior to calculation, the equation to be selected is decided. After inputting values of reaction temperature, total pressure and concentration of water vapor, the transition temperature is calculated. Then the compensation factors are read or input. In the calculation by the Langmuir-Hinshelwood eqn., a value of K_3 in the eqn. is selected from a group of several probable values to be obtain $F(P, C_{H_2O}, T)$. $R_{p,ref}$ is calculated using the necessary factors and equations.

3. Calculation of reaction rate and weight loss as a function of time

In the case of normal reactor operation, temperature, total pressure and concentration of water vapor are assumed to be constant during the reaction. The magnitude of the three kinds of factors are, however, varied with elapse time in the case of water ingress accident[6]. The calculation for such case is carried out on a assumption that only the temperature is changed during the time. The assumption above is able to give more conservative result than that under the real accident condition. After the reaction rate normalized to that at B=15 as a function of B, F(B) is

determined, changes in the reaction rate, weight loss and burn-off with the time are calculated using either the basic or modified method.

4. Calculation of burn-off profile

The burn-off value calculated above is total burn-off which does not give any information about the locality of burn-off, i.e., burn-off profile. Hence, the reaction rate and weight loss are calculated in another manner in which the burn-off profile can be obtained. On the calculating the burn-off profile, the characteristic length of oxidation, L is necessary to be much smaller than the size of component concerned. Here, the size is determined as radius for a cylindrical type and a half of thickness for a slab. Prior to calculation, we should be able to ascertain that the size of component is at least four times as small as the characteristic length of oxidation, L. Finally, the burn-off at which the component starts to erode or deteriorate at the surface is input. The weight loss is the sum of that caused by the reaction and that originated from the erosion or deterioration.
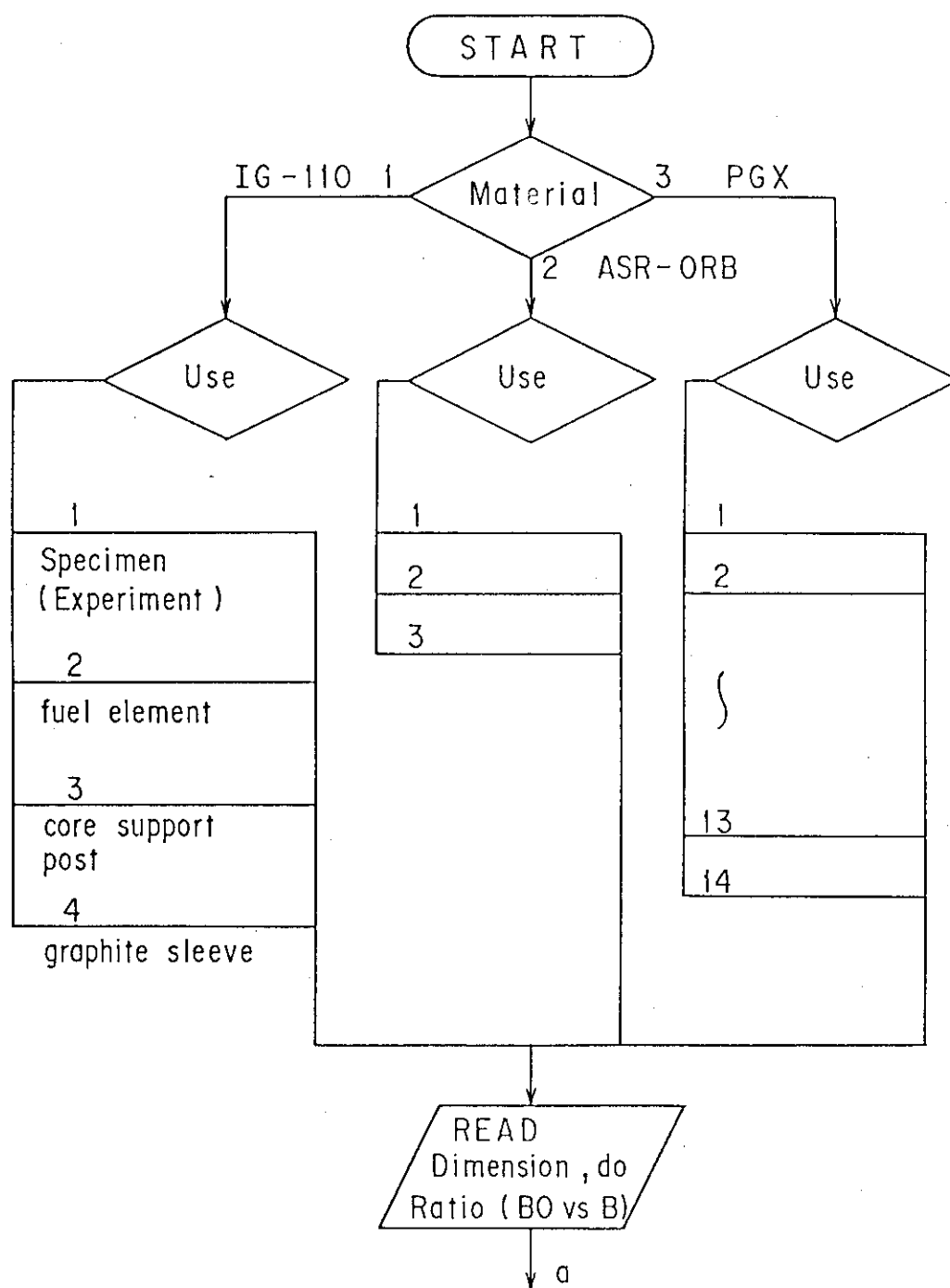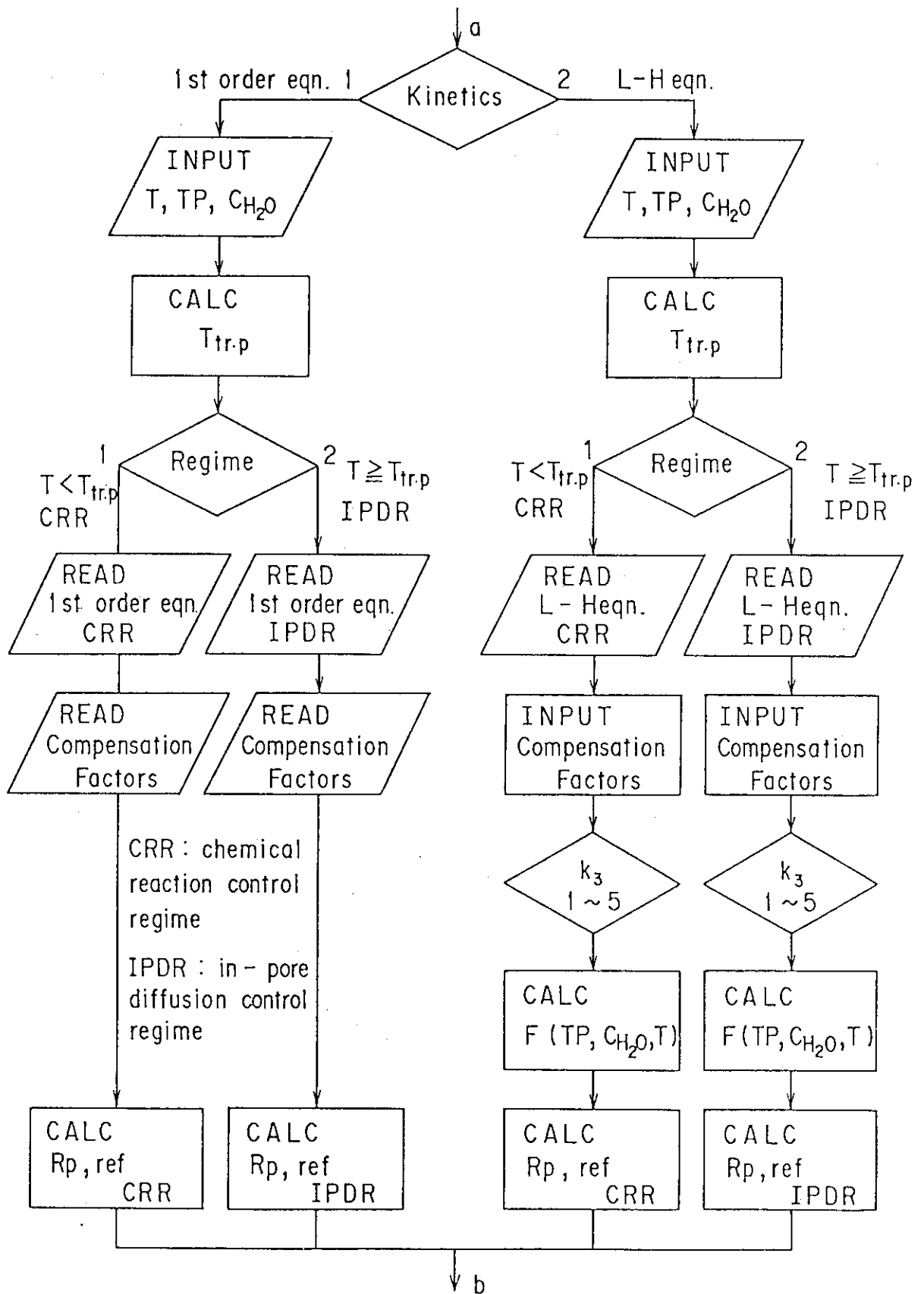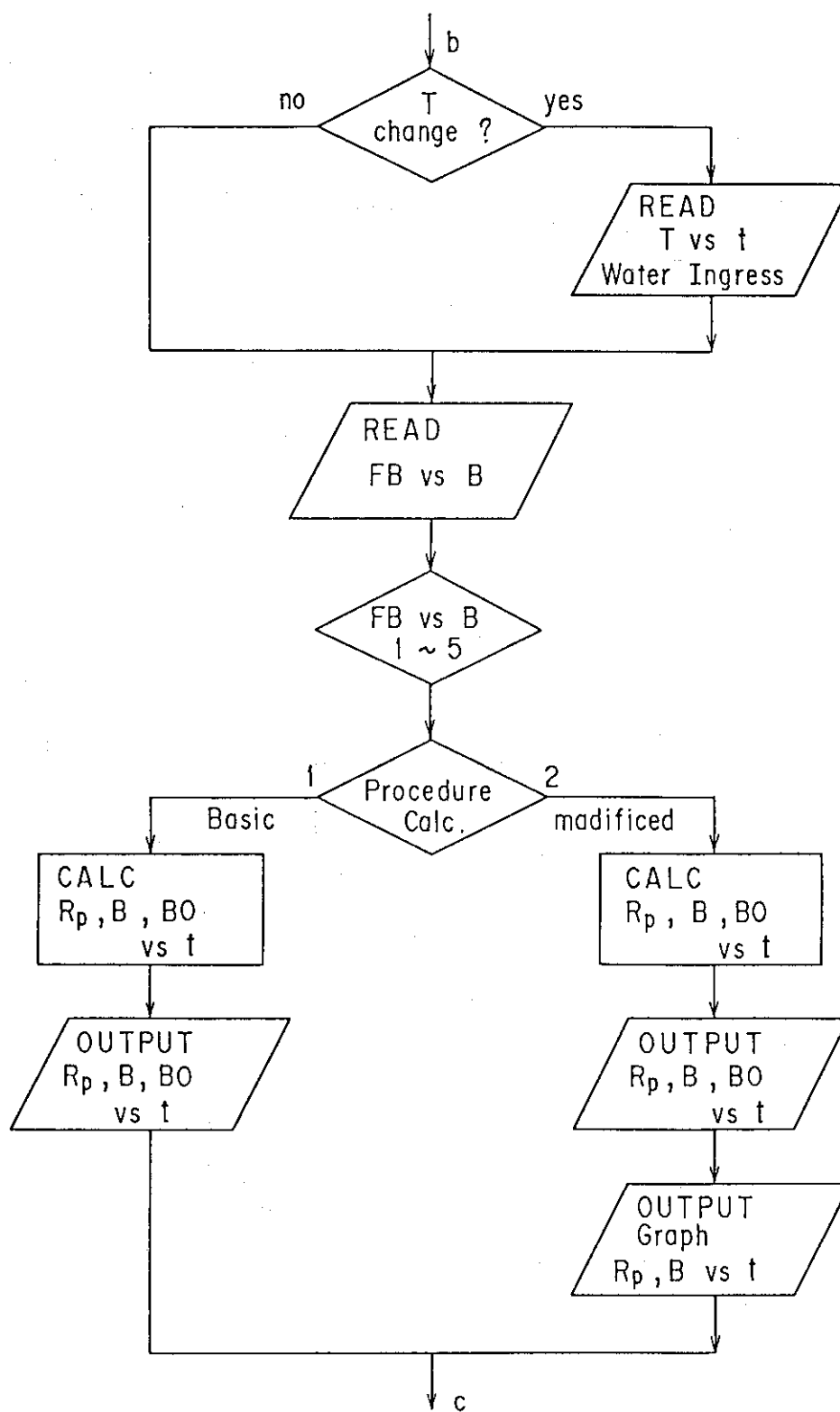
START

IG-110 1   Material   3   PGX

2   ASR-ORB

Use   Use   Use

| | |
1   1   1

| Specimen (Experiment) | | 2 | | 2 |
| 2 | | 3 | |

| fuel element | | | |
| 3 | | | |

| core support post | | | 13 |
| 4 | | | 14 |

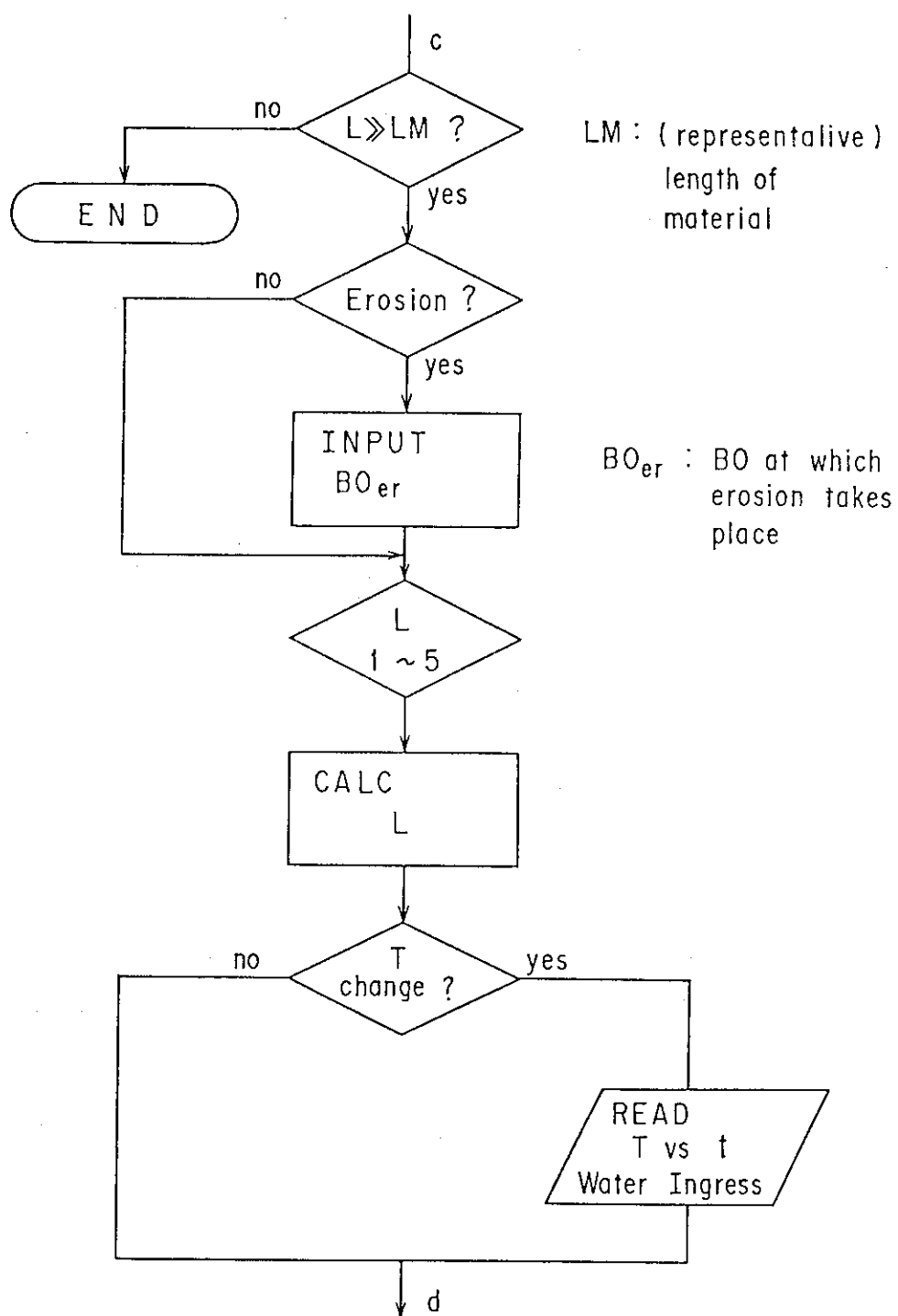graphite sleeve

READ
Dimension , do
Ratio (BO vs B)

a

Fig. A. 1 − 1

Fig. A. 1 – 2

Fig. A. 1 — 3

Fig. A. 1 — 4

Fig. A. 1 − 5